Deep mutagenesis reveals the distinct mutational landscape of ADan and ABri amyloid nucleation

Mariano Martín[1] and Benedetta Bolognesi[1]

1Institute for Bioengineering of Catalonia (IBEC), The Barcelona Institute of Science and Technology, Baldiri Reixac 10-12, 08028 Barcelona, Spain.

Abstract

Different forms of dementia are caused by stop-loss mutations in the ITM2B gene which result in the expression of 34 AA long peptides that accumulate as amyloids in human brains. In order to gather mechanistic insights into the formation of amyloids by two of these peptides, ADan and ABri - hallmarks of Danish and British dementia respectively - we employed saturation mutagenesis combined to a massively parallel selection assay that reports on amyloid nucleation. Our results reveal that ADan aggregates into amyloids remarkably faster than both the unextended peptide Bri2 and the extended ABri sequence. The complete mutational landscape of ADan reveals asparagines and charged residues as key players in the nucleation process in addition to aliphatic residues within positions 20-25. What is more, we show that extending Bri2 with just two specific residues is enough to generate a novel amyloid core which we suggest builds the structured core of ADan fibrils. On the other hand, only a handful of mutations can boost the ability of ABri to nucleate amyloids, including a SNV replacing the Bri2 stop codon by a Cys codon. Overall, the remarkably different aggregation profiles and mutational landscapes for the two peptides suggest that different disease mechanisms underlie disease in Danish and British dementia and highlight the importance of accurately measuring the impact of stop extension mutations for these and other sequences across the genome.

Intro

Amyloid deposits are the pathological signature of a wide range of human diseases mainly affecting the nervous system. The proteins that deposit in pathology are encoded by genes that are the ones mutated in familial forms of neurodegenerative diseases. Such is the case of mutations in the gene APP, the precursor of amyloid beta peptide (Aβ42), that cause familial forms of Alzheimer's disease.
Frameshift mutations and stop-loss mutations, also known as nonstop mutations, have been pin-pointed as causative variants in several pathologies (Mignogna *et al*, 2022; Bauer *et al*, 2023; Vaché *et al*, 2023; Rebelo *et al*, 2016). Nonstop mutations constitute ~0.2% of codon-changing mutations (Hamby *et al*, 2011) and often lead to mRNA degradation by the non-stop mediated-decay machinery (Monaghan *et al*, 2023). However, if an alternative in frame stop codon appears shortly afterward (within 50 nt), the 3'UTR can be translated resulting in an aberrant protein with an extended C-term

(Hamby *et al*, 2011). This is the case of a set of NEFH gene mutations that cause Charcott-Marie-Tooth disease, the most common inherited motor neuron disorder. Stop-loss mutations in the NEFH gene allow translation of cryptic amyloidogenic elements (CAEs) contained in its 3' UTR, leading to protein aggregation and neurodegeneration (Rebelo *et al*, 2016). In addition, nonstop mutations that lead to the translation of 3'UTR CAEs have been identified in the REEP1 gene in patients with peripheral neuropathy (Bock *et al*, 2018).

Preventively knowing the phenotypic impact of any genetic mutation has become a major goal of precision medicine in the era of genomics and machine learning. Many Variant Effect Predictors (VEPs) have been developed in the last years to predict the impact of missense variants (Frazer *et al*, 2021; Adzhubei *et al*, 2010; Ng & Henikoff, 2001; Brandes *et al*, 2023). However, most VEPs rely on multiple sequence alignments and cannot capture the impact of stop-loss mutations. On the other hand, amyloid aggregation predictors have also limited predictive power on these sequences. These algorithms are largely based on hydrophobicity or beta sheet propensity - features that correlate only moderately with amyloid nucleation (Seuma *et al*, 2021) - and they have been exclusively trained on single amino-acid substitutions. As a result, with the current tools, it is challenging to predict the appearance of CAEs due to stop-loss and therefore to identify potential molecular drivers of disease.

Stop-loss mutations in the gene ITM2B, also known as Bri2, have been reported in patients with rare autosomal dominant forms of dementia. Familial British Dementia (FBD), Familial Danish Dementia (FDD), as well as the recently reported Familial Chinese Dementia (FCD) and Familial Korean Dementia (FKD), are caused by mutations in this gene (Vidal *et al*, 1999, 2000; Liu *et al*, 2021; Rhyu *et al*, 2023). In FDD, a 10 nt duplication produces a C-term frameshift and concomitant stop codon loss, leading to the formation of an aberrant 34 amino acid long peptide known as ADan. In FBD, a single nucleotide variant (SNV) affects the stop codon, resulting in a stop-loss with the consequent formation of an aberrant 34 amino acid long peptide known as ABri. FCD and FKD are also caused by stop-loss mutations that produce peptides that differ from ABri only in one amino acid. Amyloid deposits formed by these aberrant peptides have been detected in patients (Holton *et al*, 2001; Ghiso *et al*, 2001; Lashley *et al*, 2006; Vidal *et al*, 2000). Both loss of function and amyloid toxicity have so far been proposed as molecular mechanisms underlying the disease, contributing to disease onset and progression (Coomaraswamy *et al*, 2010; Marcora *et al*, 2014; Tamayev *et al*, 2010a; Cantlon *et al*, 2015).

Several *in vivo* and *in vitro* approaches have been developed with the aim of understanding the molecular mechanism of aggregation that underlie these diseases. Transgenic mice expressing ADan peptide present amyloid depositions (Vidal *et al*, 2009) in contrast to mice expressing ABri peptide where no amyloids are detected (Pickford *et al*, 2006). None of the two mouse models developed for FDD recapitulates fully patient's phenotype (Vidal *et al*, 2009; Tamayev *et al*, 2010b).

In vitro studies have revealed that ABri and ADan, but not Bri2, can form toxic oligomeric species and mature fibrillar aggregates (El-Agnaf *et al*, 2001a; Gibson *et al*, 2003; El-Agnaf *et al*, 2001b; Todd *et al*, 2016; Schlenzig *et al*, 2009; Cantlon *et al*, 2015). Both

peptides exhibit an oxidized and a reduced form *in vitro*. While ADan can form toxic oligomers regardless of oxidation state, only oxidized ABri aggregates in toxic soluble oligomers (El-Agnaf *et al*, 2001a; Gibson *et al*, 2003). In solution both peptides lack a defined structure but after a few hours they evolve into beta-sheet rich structures (Todd *et al*, 2016, 2014).

While Alzheimer's disease and Bri2-related familial dementias share common clinical and neuropathological features, including amyloid depositions, the primary sequences of the amyloid-forming peptides (Aβ42 or ADan/ABri) are substantially different, making it challenging to transfer mechanistic insights acquired for Aβ42 to ADan and ABri. What is more, in contrast with Aβ42, no high-resolution structure of ADan and ABri fibrils, *in vitro* or *ex-vivo*, has been solved.

Here, we employ deep mutational scanning (DMS) to systematically study the formation of amyloids by ADan and ABri and measure the effect of all possible mutations on the respective peptide amyloid nucleation. We also quantify the effect of new stop-loss mutations, generating datasets that can be used to guide clinical interpretation of novel mutations identified in the human population. Moreover, we report that a 2 amino acid extension of Bri2 C-term is enough for producing an amyloid core that makes the peptide prone to nucleate aggregates. Finally, the resulting data provide numerous mechanistic insights into the distinct process underlying ADan and ABri fibril nucleation.

Results

Bri2 extensions differ in their nucleation propensity

We measured the effect of Bri2 extensions (Fig. 1a) on the ability of these sequences to form amyloid aggregates using a cell-based selection assay where sequences are fused to the nucleation domain of the yeast prion Sup35 (SupN) and the aggregation of the fused peptides nucleates the aggregation of endogenous Sup35, a process required for yeast growth in selective conditions (Chandramowlishwaran *et al*, 2018). Cells expressing Bri2 do not grow in these conditions, revealing that the unextended peptide does not nucleate amyloid aggregation. In sharp contrast, the expression of ADan leads to 25.14 ± 3.41% of the cells growing in selection media over non selective conditions, a 2 fold increase compared to Aβ42 (Seuma *et al*, 2021) (Fig. 1). Cells carrying ABri show very limited growth in the assay (0.0065 ± 0.0039%) with no significant difference compared to expression of the reporter without any fusion (SupN) (Fig. 1c, Supp. Fig. 1a).

ADan and ABri share the first 22 residues and differ only in the last 12 amino acids (Fig. 1a) suggesting it is the specific extension of ADan that encodes amyloid potential. Hence, we evaluated all possible ADan C-term truncations using the selection assay described above combined to deep sequencing. We designed and synthesized a library of ADan single amino acid substitutions and truncations and expressed it fused to SupN in yeast cells that went under selection. We quantified an amyloid nucleation

130 score for each variant by deep sequencing before and after selection (Fig. 1c) (Seuma
131 *et al*, 2021). We found that a Bri2 extension of just 2 amino acids (N24 and L25) is
132 enough to produce a significant increase in amyloid nucleation in comparison to Bri2
133 (Fig. 1d). This effect becomes stronger with a 3 amino acid extension (N24, L25 and
134 F26), leading to a similar nucleation score as that of the full-length ADan peptide.
135 Together with the previous observation that a 28 residue long ADan truncation forms
136 beta-sheet rich structures *in vitro* (Todd *et al*, 2016), these findings suggest that the
137 amyloid potential of ADan is encoded by the first residues that get translated upon
138 stop-loss.
139
140 **Deep mutagenesis of ADan**
141 To investigate and compare the effects of diverse genetic variants on the aggregation
142 of ADan we then looked at the impact of all possible single amino acid changes in the
143 ADan sequence by the same approach. The resulting nucleation scores are
144 reproducible between replicates (Fig. 2a, Supp. Fig. 1c) and correlate well with the
145 effects of variants quantified individually (R = 0.94, p-value<0.01, Fig.2b). Growth of
146 cells expressing Bri2, ABri or ADan fusions in non selective conditions revealed that
147 their growth rates were not confounded by differential toxicity.
148 Altogether, we measured amyloid nucleation for 677 variants. The distribution of
149 mutational effects for ADan nucleation has a strong bias towards reduced amyloid
150 nucleation, with 44% of single amino acids substitutions reducing nucleation but only
151 25% increasing it (Z-test, false discovery rate [FDR] = 0.1, Fig. 2c,d). Among the
152 variants that decrease nucleation, 66 have nucleation scores similar to mean Bri2-
153 truncations nucleation score. Finally, 200 variants have a nucleation score similar to
154 WT ADan.
155
156 **ADan nucleation core is a product of Bri2 extension**
157 Inspecting the heatmap of mutational effects for amino acid changes at all positions in
158 ADan reveals that most of the mutations that decrease amyloid nucleation are
159 localized between residues L20-L25 (Fig. 2e, Supp. Fig. 2). As in this continuous
160 stretch of residues most of the mutations decrease amyloid nucleation and all
161 substitutions to prolines here disrupt nucleation, we propose that this region forms the
162 inner core of ADan fibrils. In particular, the most important residue of the core seems
163 to be N24 as all mutations at this position lead to a decrease in nucleation. Charges
164 in this region are not allowed, except at position 23. The two residues that precedes
165 the core (E18 and T19) are also important as many of the mutations (mainly to
166 hydrophobic amino acids) at these positions decrease nucleation. Albeit, distant from
167 this region, residues N4 and E31 are also crucial for the nucleation of ADan as most
168 substitution of these residues decrease nucleation suggesting longer distance
169 interactions with residues of the amyloid core or a role in modulating the conformations
170 of the monomeric ADan ensemble. Overall, asparagines and glutamic acids are key
171 in ADan nucleation as most substitutions of these amino acids decrease nucleation
172 (Fig. 2f).
173

174 **ADan gatekeeper residues**
175 We consider as gatekeeper those positions where mutations are more likely to
176 increase nucleation rather than decrease it. We identified 5 residues as gatekeepers:
177 F6 (12 mutations increasing nucleation and 2 decreasing), I8 (15 increasing), K14 (11
178 increasing and 2 decreasing), A16 (12 increasing and 5 decreasing) and L27 (11
179 increasing and 3 decreasing) (Fig.2e). Surprisingly, and in contrast to Aβ42 (Seuma
180 eLife), the gatekeepers are all aliphatic residues with the exception of K14.
181
182 **Combination of SNPs and FDD mutation affects ADan nucleation propensity**
183 14 SNPs are reported for *bri2* in the GnomAD database (Chen *et al*, 2022) that affect
184 the C-term of this protein and 8 SNPs in the 3' UTR (up to ABri stop codon) (Supp.
185 Table 1). We asked what the impact of these SNPs would be in combination with the
186 10 nt duplication that leads to the ADan peptide formation. Most of the SNPs in the
187 context of ADan peptide decrease nucleation or do not affect the nucleation of the
188 peptide. Only two of the reported SNPs (rs1272422512 and rs1455609180), that result
189 in R9Q and K32T mutations, increase nucleation. However, we identify another 53
190 SNVs that are able to significantly increase nucleation in ADan, providing a
191 comprehensive atlas for the evaluation of genetic variation in this sequence.
192
193 **Bri2 stop-loss mutations, different to FBD, increase nucleation**
194 We then employed the same strategy for studying the effect of diverse ABri genetic
195 variants on amyloid nucleation. As the expression of ABri - and its saturation
196 mutagenesis library - result in limited growth in the selection assay, we applied a
197 stringent filter in order to proceed with analysis only with those variants that have a
198 low normalized sigma value (see Methods, Supp. Fig. 1c) and thus, an accurate
199 estimate. Most of the confident variants are those that increase nucleation. The
200 resulting nucleation scores are reproducible between replicates (Fig. 3a, Supp. Fig.
201 1d) and correlate well with the effects of variants quantified individually (R = 0.83,
202 Fig.3b). The heatmap of mutational effects for amino acid changes at all positions in
203 ABri reveals that substitutions R24L and R24S increase nucleation (Fig. 3c, Supp. Fig.
204 2b), meaning that the peptides that are a product of FCD and FKD mutations are more
205 prone to aggregate than ABri. ABri stop-loss due to SNVs can lead to stop codon
206 substitution by R (FBD), L (FCD), S (FKD), G, W or C. SNV stop-loss leading to G at
207 position 24 of the extended peptide does not differ from ABri nucleation propensity.
208 However, a C at position 24 significantly increases nucleation. When tested
209 individually, the strength of R24C nucleation is half of Aβ42 nucleation and 25% of that
210 of ADan (Fig. 3b,c). 10 out of 11 substitutions, beyond SNVs, at position 24 increase
211 nucleation, revealing that R24 may act as a gatekeeper of ABri nucleation. In addition,
212 residue N13 is also a candidate gatekeeper as any change at this position increases
213 ABri nucleation.
214
215 **Mutation L20C severely increase ABri nucleation**
216 A particular mutation in ABri is the strongest nucleator of this library: L20C (Fig. 3c).
217 Cells expressing this ABri mutant have a relative growth rate (colonies in selective

condition / colonies in non-selective conditions) of 63.1 ± 7.1% (-URA-Ade/-URA), 2.7 times more than ADan peptide (23.1 ± 3.6%), confirming that this sequence is a very fast nucleator.

ADan nucleation is different from Aβ42 and ABri nucleation

In order to evaluate if the impact of mutations on amyloid nucleation of ADan depends on similar properties as those driving Aβ42 nucleation, we compared the nucleation scores obtained after mutagenizing both peptides. There is no significant correlation between the nucleation of these peptides when comparing the effect of specific amino acid changes (Fig. 4a), as well as mutations from the same amino acid (Fig. 4b) and mutations to the same amino acid (Fig. 4c). In addition, to compare mutational effect per position, we aligned ADan and Aβ42 peptides in three different ways, at the N-term, C-term and with ClustalO (Madeira *et al*, 2022). Regardless of the strategy, no significant correlation at the aligned positions was detected (Supp. Fig. 3a,b,c).
Similarly, we compared ADan and ABri nucleation scores. None of the comparisons between ADan and ABri revealed significant correlations between the nucleation scores of these peptides (Fig. 4d,e; Supp. Fig. 3d). We also tested the correlation in those positions where we have at least 5 confident measurements in the ABri library (Fig. 4f) uncovering significant positive correlations only for positions 13 (N), 26 (F and V) and 32 (K and E, ADan and ABri respectively).

Structural insights may explain the difference in aggregation propensity between Bri2 extended peptides

In ADan, substitutions to prolines increase nucleation up to residue 21 but between residues 21-26 (where we propose that the amyloid core is located) decrease nucleation. This increase in nucleation due to proline substitution in the first part of the peptide may suggest the presence of secondary structure elements in monomeric ADan that would be able to prevent nucleation. Thereafter, we used state-of-the-art structure predictors for predicting Bri2, ABri and ADan structures. Alphafold and ESM (Jumper *et al*, 2021; Lin *et al*, 2023) predict Bri2 structure as a beta-hairpin and ABri structure as a beta-sheet or a beta-hairpin with a disordered tail (Supp. Fig. 4a,b). While there is consensus between predictors for Bri2 and ABri, the outcome is different when it comes to ADan, that is predicted as a beta-hairpin with a disordered tail with a small helix (low confidence in this region) by Alphafold and as two helices (low confidence) by ESM. This may suggest that Bri2 and ABri have more stable native structures, while ADan may sample a higher energy ensemble of conformations. In order to explore these ensembles of configurations, we used the CALVADOS coarse-grained force field (Tesei & Lindorff-Larsen, 2023) to run dynamic simulations of Bri2, ABri and ADan peptides.The nonionic energy contact map for ADan reveals a cluster of interactions between residues 5-11 with residues 19-28 (Supp. Fig. 4C). In contrast, the energy contact map for ABri shows a smaller cluster of interactions that comprehends residues 6-11 and 19-24. Bri2, has an even smaller cluster of interactions that is similar to the one of ABri. While residues F6, A7 and I8 are close to residues L20 and I21 in the predicted ABri three dimensional structures, when it

262 comes to ADan a larger set of favorable pair-wise interactions are predicted by
263 CALVADOS force field and may contribute to overcome the energy barrier to ADan
264 nucleation.
265
266
267 **Discussion**
268
269 Bri2 gene mutations affecting its stop codon are associated with familial forms of
270 dementia: FBD, FDD, FCD and FKD. Upon furin processing and cleavage, these
271 mutations lead to the production of aberrant C-term extended peptides known as ABri
272 and ADan (FBD and FDD, respectively) which form amyloid aggregates in the affected
273 individuals (Vidal *et al*, 1999, 2000).
274 The resulting toxicity is proposed to depend both on the reduced expression of the
275 precursor protein (Tamayev *et al*, 2010b, 2010a) and by the fate of the cleaved
276 sequences. Both ADan and ABri, as well as the peptides generated in FCD and FKD,
277 are 34 amino acids long. While the sequence of the first 22 residues is common, these
278 peptides differ in the last 12 C-terminal residues.
279 The clinical features of these forms of dementias are strikingly similar to those of AD,
280 suggesting a similar gain of toxic function mechanism upon mutation, but the primary
281 sequences of ADan and ABri differ entirely from that of Aβ42, posing the question of
282 how these sequences aggregate. In order to systematically measure the formation of
283 amyloids by these two distinct peptides and to gather mechanistic insights on how they
284 turn into amyloids upon extension, we combined DMS to a selection assay that reports
285 on amyloid nucleation and obtained a comprehensive mutational landscape of the two
286 peptides. The reporter assay revealed that Bri2, ABri and ADan peptides have
287 different nucleation propensity. Bri2 has no signal in the cell-based assay, meaning
288 that the 23 amino acid long peptide is not nucleating amyloid aggregates. While ADan
289 peptide very rapidly forms amyloids in the cell-based assay, 2 fold faster than Aβ42
290 for reference, ABri is at the lower end of the detection capability of the assay.
291 In both FBD and FDD patients amyloid depositions formed by the aberrant peptides
292 have been detected (Vidal *et al*, 1999, 2000), revealing that both peptides can nucleate
293 amyloid aggregation. However, the difference we measure is in line with mice models
294 for FBD and FDD. Transgenic mice expressing ABri do not exhibit amyloid depositions
295 (Pickford *et al*, 2006) while those expressing ADan feature parenchymal amyloid
296 deposition and cerebral amyloid angiopathy (Vidal *et al*, 2009). Furthermore, there's
297 evidence for ADan leading to higher toxicity than ABri in a *Drosophila* model, possibly
298 due to a faster rate of aggregation of the ADan peptide (Marcora *et al*, 2014).
299 The low nucleation rate of the ABri peptide in our assay suggests a more drastic
300 difference in aggregation rates of the two peptides than what has been proposed from
301 *in vitro* experiments so far. The ability of both peptides to aggregate into beta-sheet
302 rich aggregates has been observed *in vitro* (Todd *et al*, 2016, 2014), but there is no
303 quantitative comparison reporting on the aggregation kinetics of these two peptides,
304 i.e. on how fast they nucleate amyloids. The aggregation propensity of these peptides
305 is also thought to be affected by post-translational modifications such as the N-term

306 glutamate to pyroglutamate conversion, disulfide bond formation and truncations.
307 However, pyroglutamate formation is not compatible with the nucleation assay
308 employed here as the peptide N-term is engaged in the SupN fusion. Moreover, the
309 reporter assay takes place in the yeast cytosol making the formation of disulfide bonds
310 unlikely. *In vitro*, it has been shown that only the oxidized form of ABri aggregates in
311 toxic soluble oligomers (El-Agnaf *et al*, 2001a). In contrast, both ADan oxidized and
312 reduced forms can form oligomers, with the reduced form resulting in higher
313 neurotoxicity (Gibson *et al*, 2003).
314
315 In ADan, we identify a continuous stretch of residues (L20-L25) that are crucial for
316 amyloid nucleation as most amino acid changes at these positions decrease
317 nucleation. This region contains four aliphatic residues that together with polar and
318 charged residues (N4, E12, N13 and E31) are likely to be involved in the amyloid
319 interface at the core of the aggregates formed by this peptide. Surprisingly, and in
320 contrast to Aβ42, gatekeeper residues in ADan are mainly hydrophobic (F6, I8, A16
321 and L27), with the exception of K14.
322 Overall, correlating nucleation scores for the same types of mutation reveals that the
323 nucleation of amyloids by ADan differs from Aβ42, as well as from ABri. ADan amyloid
324 formation is also not exclusively hydrophobicity driven (Supp. Fig. 5), and as
325 previously mentioned, it rather involves polar and negative charged residues. It would
326 have been impossible to predict the types of changes that increase or decrease
327 nucleation in Adan even on the basis of the complete mutational dataset of Aβ42
328 nucleation (Seuma *et al*, 2022), highlighting the need of systematically measuring
329 amyloid nucleation for these and other peptides that are known to result in similar
330 phenotypes (Seuma & Bolognesi, 2022).
331
332 The low signal/noise ratio for ABri also makes it difficult to identify positions where
333 mutations disrupt amyloid formation and therefore where a likely fibril core could be
334 established. However, we can still confidently identify those positions where single
335 amino acid substitutions are more likely to increase ABri nucleation. Of special interest
336 and concern are mutations affecting the position R24 as this is the position coded by
337 the mutation in the original stop codon. FCD and FKD mutations (R24L and R24S)
338 increase nucleation of ABri peptide. The R24C substitution here, which results from a
339 SNV affecting the stop codon, severely increases nucleation generating one of the
340 strongest nucleators in the ABri library together with L20C. Both substitutions occur at
341 a two residue distance from Cys22, forming a Cys-X-Cys motif. This type of motif can
342 bind metal ions as zinc or copper (Scheller *et al*, 2018) and modulate amyloid nucleation.
343 Alternatively, Cys-Cys ladders in the fibril axis could stabilize the amyloid
344 conformation, as reported in other amyloid-forming sequences (Mompeán *et al*, 2018).
345 Overall, ~90% of the mutations of R24 quantified here increase nucleation, with 8
346 mutations, besides those leading to FCD and FKD, that are likely to be pathogenic.
347 This suggests that the majority of extensions of Bri2 resulting from stop-loss are of
348 concern.
349

Circular Dichroism experiments revealed that, before evolving into beta-sheet rich structures, ABri and ADan are largely disordered (Todd *et al*, 2016, 2014). On the other hand, structure predictions using Alphafold and ESM show a consensus for Bri2 and ABri peptides, with predicted beta strands, but not for ADan. It is possible that Bri2 and ABri may populate a more stable ensemble of conformations in their monomeric state, while ADan could more easily overcome the energy barrier to amyloid nucleation. Dynamic simulations using the CALVADOS force field (Tesei & Lindorff-Larsen, 2023) reveal energetically favorable interactions between residues 5-11 and 19-28 in ADan and between shorter stretches in ABri (residues 6-11 and 19-24), some of which could be prone to nucleate amyloid fibril formation. In the lack of a clear consensus, even on the basis of the most advanced structure prediction tools (Jumper *et al*, 2021; Lin *et al*, 2023), datasets such as the ones generated here can be of great help to guide or re-train structural and molecular dynamics models for these peptides.

The Bri2 gene presents several SNPs reported in GnomAD (Chen *et al*, 2022). Among them, 14 occur before position 23 of the cleaved peptide and 8 in the 3'UTR, in the region that gets translated as the novel C-term of the extended peptides. It is plausible that a person carries one of the reported SNPs in combination with a stop-loss mutation. SNPs mutation in the ADan background do not increase nucleation, except for R9Q (rs1272422512) and K32T (rs1455609180). In contrast, in ABri background 4 SNPs can increase nucleation: A7S (rs578006622), I8V (rs139394220), L20S (rs1428007068) and K28R (rs760120359). The remaining SNPs do not have effect on the nucleation of these peptides or can even decrease it, therefore acting as protective variants.

TGA is the most susceptible codon to stop-codon readthrough, a phenomenon which happens at low frequency of 0.01-0.1% (Floquet *et al*, 2012; Dabrowski *et al*, 2015), and that can cause an extension of Bri2 at the C-terminus. In this scenario the resulting Bri2 extended peptide would be similar to the ABri peptide. This mechanism can be promoted by small molecules such as Gentamycin or 5-Fluoruridine, drugs that are already used as treatment for different conditions (Toledano *et al*, 2023). Patients under treatment with these drugs may be suffering stop-codon readthrough and, the translation of CAEs that may drive amyloid fibrils aggregation.

Mapping the effects of all ADan truncation shows that a Bri2 two amino acid extension is enough for increasing nucleation in comparison to Bri2 peptide. A three amino acid extension severely increases nucleation. A similar increase in nucleation is seen for the remaining truncations. These results are in agreement with a previous study showing that an ADan truncation at position 28 can form beta-sheet rich structures *in vitro* (Todd *et al*, 2016). Our results reveal that the nucleation core is likely formed by this short extension itself and highlights the importance of studying other possible Bri2 extensions that may play important roles in the development of dementia.

Furthermore, our research reinforces the importance of studying CAEs coded in 3' UTRs as firstly proposed by Rebelo *et al* (Rebelo *et al*, 2016). Stop-loss can lead to the translation of CAEs that may be the driving force of neurodegenerative disease or

394 systemic amyloidosis. Rebelo *et al.*Haga clic o pulse aquí para escribir texto.identified
395 CAEs in NEFH, NEFL and FUS 3' UTRs by using a range of amyloid aggregation
396 predictors. However, the output scores of these tools poorly correlate with nucleation
397 scores. This is likely due to the fact that these predictors were trained on a small
398 number of sequences and are based exclusively on hydrophobicity scores or beta-
399 sheet propensity features that alone cannot explain amyloid nucleation. Indeed, here
400 we show the relevance of polar and charged residues in ADan amyloid nucleation.
401 Thus, a systematic and high-throughput identification of CAEs is needed as it will open
402 new avenues for the understanding of familial amyloidosis.
403
404
405
406 **Methods**
407
408 **Library design**
409 The designed libraries contain a total of 1088 unique ADan nucleotide variants (680
410 single protein variants encoded by 1, 2, and 3 nucleotide changes) and 1088 unique
411 ABri nucleotides variants (680 single protein variants encoded by 1, 2, and 3
412 nucleotide changes).
413
414 **Plasmid Library construction**
415 Libraries were synthesized by Integrated DNA Techonologies (IDT) as oligo pools
416 covering the ADan and/or ABri 102 nt sequence, flanked by 25 nt upstream and 21 nt
417 downstream constant regions for cloning. 10 ng of the library were amplified by PCR
418 (Q5 high-fidelity DNA polymerase, NEB) for 12 cycles with primers annealing to the
419 constant regions (primers MM_01-02, Supplementary Data 2). The product was
420 purified from a 2% agarose gel (QIAquick Gel Extraction Kit, Qiagen). In parallel, the
421 PCUP1-Sup35N plasmid was linearized by PCR (Q5 high-fidelity DNA polymerase,
422 NEB; primers MM_03-04, Supplementary Data 2). The product was purified from a 1%
423 agarose gel (QIAquick Gel Extraction Kit, Qiagen). The oligo pool was then ligated into
424 200 ng of the linearized plasmid in a 1:10 (vector:insert) ratio by a Gibson approach
425 with 3 h of incubation followed by dialysis for 3 h on a membrane filter (MF-Millipore
426 0.025 µm membrane, Merck) and vacuum concentration. The product was
427 transformed into 10-beta Electrocompetent E. coli (NEB), by electroporation with 2.0
428 kV, 200 Ω, 25 µF (BioRad GenePulser machine). Cells were recovered in SOC
429 medium for 30 min and grown overnight in 30 ml of LB ampicillin medium. A small
430 amount of cells were also plated in LB ampicillin plates to assess transformation
431 efficiency. A total of >1M transformants were estimated, meaning that each variant in
432 the library is represented ~1000 times. 5 ml of overnight culture were harvested to
433 purify the library with a mini prep (QIAprep Miniprep Kit, Qiagen).
434
435 **Yeast transformation**
436 Saccharomyces cerevisiae [psi-pin-] (MATa ade1–14 his3 leu2-3,112 lys2 trp1 ura3–
437 52) provided by the Chernoff lab (Chandramowlishwaran *et al*, 2018) was used in all

438 experiments in this study. Yeast cells were transformed with the libraries in three
439 biological replicates. Per replicate, an individual colony was grown overnight in 3 ml
440 YPDA medium at 30 °C and 4 g. Cells were diluted in 40 ml to OD600 = 0.3 and grown
441 for 4–5 h. When cells reached the exponential phase (OD~0.8–0.9) cells were
442 harvested at 3000 × g for 5 min, washed with 50 ml milliQ, centrifuged at 3000 × g for
443 5 min and washed with 25 ml SORB buffer (100mMLiOAc, 10mMTris pH 8.0,
444 1mMEDTA, 1M sorbitol). Cells were resuspended in 1.4 ml of SORB and incubated
445 30 min on an orbital shaker. After incubation, 800 ng of library and 30 ul of ssDNA (
446 UltraPure, Thermo Scientific) were added and incubated for 5 min at room temperature
447 and then 10 min on an orbital shaker. 6 ml of YTB-PEG (100mM LiOAc, 10mM Tris
448 pH 8.0, 1mM EDTA, 40% PEG 3350) and 580 ul of DMSO were added to the cells.
449 Heat-shock was performed at 42 °C for 20 min in a liquid bath with intermittent shaking.
450 Cells were harvested and incubated in 50 ml of recovery medium (YPDA medium +
451 Sorbitol 0.5 M) for 1 h at 30 °C. Cells were harvested and grown in 50 ml plasmid
452 selection medium (-URA, 2% glucose) for 50 h at 30 °C. A small amount of cells were
453 also plated in plasmid selection medium to assess transformation efficiency. 60,000-
454 100,000 transformants were estimated for each biological replicate, meaning that each
455 variant in the library is represented at least 50 times. After 50 h, cells were diluted in
456 50 ml plasmid selection medium to OD= 0.05 and grown exponentially for 15 h. Finally,
457 the culture was harvested and stored at −80 °C in 25 % glycerol.
458
459 **Selection experiments**
460 *In vivo* selection assays were performed in three biological replicates. For each
461 technical replicate, cells were thawed from −80 °C in 50 ml plasmid selection medium
462 at OD = 0.05 and grown until exponential for 15 h. At this stage, cells were harvested
463 and resuspended in 50 ml protein induction medium (-URA, 2% glucose, 100
464 µMCu2SO4) at OD = 0.1. After 24 h the 40 ml input pellets were collected and cells
465 were plated on -ADE-URA selection medium in 145-cm2 plates (Nunc, Thermo
466 Scientific). Plates were incubated at 30 °C for 7 days. Finally, colonies were scraped
467 off the plates with PBS 1x and harvested by centrifugation to collect the output pellets.
468 Both input and output pellets were stored at −20 °C before DNA extraction.
469
470 **DNA extraction and sequencing library preparation**
471 One input and one output pellets for each biological replicate were resuspended in
472 0.5ml extraction buffer (2% Triton-X, 1% SDS, 100mMNaCl, 10mMTris-HCl pH 8,
473 1mM EDTA pH 8). They were then freezed for 10 min in an ethanol-dry ice bath and
474 heated for 10 min at 62 °C. This cycle was repeated twice. 0.5ml of
475 phenol:chloroform:isoamyl (25:24:1 mixture, Thermo Scientific) was added together
476 with glass beads (Sigma). Samples were vortexed for 10 min and centrifuged for 30
477 min at 2000 × g. The aqueous phase was then transferred to a new tube, and mixed
478 again with phenol:chloroform:isoamyl, vortexed and centrifuged for 45 min at 2000 ×
479 g. Next, the aqueous phase was transferred to another tube with 1:10 V 3M NaOAc
480 and 2.2 V cold ethanol 96% for DNA precipitation. After 30 min at −20 °C, samples
481 were centrifuged and pellets were dried overnight. The following day, pellets were

482 resuspended in 0.3ml TE 1X buffer and treated with 10 µl RNAse A (Thermo Scientific)
483 for 30 min at 37 °C. DNA was finally purified using 10 µl of silica beads (QIAEX II Gel
484 Extraction Kit, Qiagen) and eluted in 30 µl elution buffer. Plasmid concentrations were
485 measured by quantitative PCR with SYBR green (Merck) and primers annealing to the
486 origin of replication site of the PCUP1-Sup35N plasmid at 58 °C for 40 cycles (primers
487 MM_05-06, Supplementary Data 2). The library for high-throughput sequencing was
488 prepared in a two-step PCR (Q5 high-fidelity DNA polymerase, NEB). In PCR1, 50
489 million of molecules were amplified for 15 cycles with frame-shifted primers with
490 homology to Illumina sequencing primers (primers MM_07–20, Supplementary Data
491 2). The products were purified with ExoSAP treatment (Affymetrix) and by column
492 purification (MinElute PCR Purification Kit, Qiagen). They were then amplified for 12
493 cycles in PCR2 with Illumina-indexed primers (primers MM_21–37, Supplementary
494 Data 2). The six samples of each replicate were pooled together equimolarly and the
495 final product was purified from a 2% agarose gel with 20 µl silica beads (QIAEX II Gel
496 Extraction Kit, Qiagen). The library was sent for 125 bp paired-end sequencing in an
497 Illumina HiSeq2500 sequencer at the CRG Genomics core facility. In total, >50 million
498 paired-end reads were obtained representing >1000x read coverage for each
499 designed variant in the library.
500
501 **Individual variant testing**
502 Selected variants for individual testing were obtained by PCR linearisation (Q5 high-
503 fidelity DNA polymerase, NEB) with mutagenic primers (primers MM_38-59,
504 Supplementary Data 2). PCR products were treated with Dpn1 overnight and
505 transformed in DH5α competent E.coli. Plasmids were purified by mini prep (QIAprep
506 Miniprep Kit, Qiagen) and transformed into yeast cells All mutated plasmids were
507 verified by Sanger sequencing. For measuring growth in selective conditions, yeast
508 cells expressing individual variants were grown overnight in a plasmid selection
509 medium (-URA 2% glucose). They were then diluted to OD 0.1 in protein induction
510 medium (-URA 2% glucose 100 µM Cu2SO4) and grown for 24 h. Cells were plated
511 on -URA (control) and -ADE-URA (selection) plates in three independent replicates,
512 and allowed to grow for 7 days at 30 °C. Adenine growth was calculated as the
513 percentage of colonies in -ADE-URA relative to colonies in -URA.
514
515 **Data processing**
516 FastQ files from paired end sequencing of the libraries were processed using DiMSum
517 (https://github.com/lehner-lab/DiMSum) (Faure *et al*, 2020), an R pipeline for analyzing
518 deep mutational scanning data. 5′ and 3′ constant regions were trimmed, allowing a
519 maximum of 20% of mismatches relative to the reference sequence. Sequences with
520 a Phred base quality score below 30 were discarded. Non-designed variants were also
521 discarded for further analysis, as well as variants with fewer than 200 input reads in
522 all of the replicates. Estimates from DiMSum were used to choose the filtering
523 thresholds.
524
525 **Nucleation scores and error estimates**

The DiMSum package (https://github.com/lehner-lab/DiMSum) (Faure *et al*, 2020) was also used to calculate nucleation scores (NS) and their error estimates for each variant in each biological replicate as:

$$\text{Nucleation score} = ESi - ESwt$$

Where ESi = log(Fi OUTPUT) - log(Fi INPUT) for a specific variant and ESwt = log(Fwt OUTPUT) - log(Fwt INPUT) for ADan or ABri WT.

NSs for each variant were merged across biological replicates using error-weighted mean and centered to the WT NS. All NS and associated error estimates are available in Supplementary Data 1.
ADan library has a good signal/noise ratio due to its significant growth in the selection assay. After NSs centering, each variant was tested against the WT NS at FDR=0.1 and classified in three possible groups: WT-like, NS_inc and NS_dec. Sigma values were normalized to the interquartile range and WT-like variants with a normalized sigma value above a cut-off of 0.2 were excluded. The same procedure was part of ABri library processing, but as it has a poor signal/noise ratio a more stringent filtering process was applied. Only those variants with a normalized sigma value <=0.2 were kept and analyzed.

Data analysis

Variants in the library. NS was obtained for 677 unique ADan variants and 679 unique ABri variants. 664 confident estimates were obtained for the ADan library and 177 in the ABri library.

Aggregation and variant effect predictors. For the aggregation predictors (Tango, Amypred, Camsol) (Fernandez-Escamilla *et al*, 2004; Charoenkwan *et al*, 2022; Sormanni *et al*, 2015), individual residue level scores were summed to obtain a score per single AA mutation sequence. We also used the Kyte-Doolittle hydrophobicity scale (Kyte & Doolittle, 1982).

Structural analysis

Structure prediction was performed using AlphaFold2 colab (https://colab.research.google.com/github/sokrypton/ColabFold/blob/main/AlphaFold2.ipynb#scrollTo=33g5IIegij5R) (Mirdita *et al*, 2022) and ESM (https://esmatlas.com/) (Lin *et al*, 2023). 3D structures were visualized using Visual Molecular Dynamics software (VMD) (Humphrey *et al*, 1996).
Molecular dynamic simulations were run in the IDR.lab colab (https://colab.research.google.com/github/KULL-Centre/EnsembleLab/blob/main/IDRLab.ipynb#scrollTo=-SCC7r8ItUTy) (Tesei *et al*, 2023).

Statistics and reproducibility

Based on the transformation efficiency, each variant in the designed libraries (n = 1088 nucleotide variants each) is expected to be represented at least 10x at each step-in

570 selection experiments and library preparation. In terms of sequencing, reads that did
571 not pass the QC filters using the DiMSum package were excluded
572 (https://github.com/lehner-lab/DiMSum) (Faure *et al*, 2020). The experiments were not
573 randomized. The Investigators were not blinded to allocation during experiments and
574 outcome assessment.
575
576 **Data availability**
577 Raw sequencing reads and processed nucleation scores are deposited in GEO and
578 can be accessed through reviewer token. The processed reads and nucleation scores
579 are also available as Supplementary Table 1.
580
581 **Acknowledgements**
582 Work in the lab of BB is supported by the la Caixa Research Foundation project
583 'DeepAmyloids' (LCF/PR/HR21/52410004), by the Spanish Ministry of Science,
584 Innovation and Universities (PID2021-127761OB-I00 and RYC2020-028861-I, funded
585 by MCIN/AEI/ 10.13039/501100011033, "ERDF A way of making Europe" and "ESF
586 Investing in your future"). IBEC is a member of the CERCA Program / Generalitat de
587 Catalunya. We thank the Chernoff lab for providing strains and plasmids and the CRG
588 Genomics core technology for sequencing.
589
590
591
592 **References**
593
594 Adzhubei IA, Schmidt S, Peshkin L, Ramensky VE, Gerasimova A, Bork P, Kondrashov AS
595 & Sunyaev SR (2010) A method and server for predicting damaging missense
596 mutations. *Nat Methods* 7: 248–249
597 Bauer AH, Basta DW, Hornick JL & Dong F (2023) Loss of function SMAD4 nonstop
598 mutations in human cancer. *Histopathology* 82: 1098–1104
599 Bock AS, Günther S, Mohr J, Goldberg L V., Jahic A, Klisch C, Hübner CA, Biskup S &
600 Beetz C (2018) A nonstop variant in *REEP1* causes peripheral neuropathy by
601 unmasking a 3′UTR-encoded, aggregation-inducing motif. *Hum Mutat* 39: 193–196
602 Brandes N, Goldman G, Wang CH, Ye CJ & Ntranos V (2023) Genome-wide prediction of
603 disease variant effects with a deep protein language model. *Nat Genet* 55: 1512–1522
604 Cantlon A, Frigerio CS, Freir DB, Boland B, Jin M & Walsh DM (2015) The Familial British
605 Dementia Mutation Promotes Formation of Neurotoxic Cystine Cross-linked Amyloid Bri
606 (ABri) Oligomers. *Journal of Biological Chemistry* 290: 16502–16516
607 Chandramowlishwaran P, Sun M, Casey KL, Romanyuk A V., Grizel A V., Sopova J V.,
608 Rubel AA, Nussbaum-Krammer C, Vorberg IM & Chernoff YO (2018) Mammalian
609 amyloidogenic proteins promote prion nucleation in yeast. *Journal of Biological*
610 *Chemistry* 293: 3436–3450
611 Charoenkwan P, Ahmed S, Nantasenamat C, Quinn JMW, Moni MA, Lio' P &
612 Shoombuatong W (2022) AMYPred-FRL is a novel approach for accurate prediction of
613 amyloid proteins by using feature representation learning. *Sci Rep* 12: 7697

614 Chen S, Francioli LC, Goodrich JK, Collins RL, Kanai M, Wang Q, Alföldi J, Watts NA, Vittal
615 C, Gauthier LD, *et al* (2022) A genome-wide mutational constraint map quantified from
616 variation in 76,156 human genomes. *bioRxiv*: 2022.03.20.485034
617 Coomaraswamy J, Kilger E, Wölfing H, Schäfer C, Kaeser SA, Wegenast-Braun BM,
618 Hefendehl JK, Wolburg H, Mazzella M, Ghiso J, *et al* (2010) Modeling familial Danish
619 dementia in mice supports the concept of the amyloid hypothesis of Alzheimer's
620 disease. *Proceedings of the National Academy of Sciences* 107: 7969–7974
621 Dabrowski M, Bukowy-Bieryllo Z & Zietkiewicz E (2015) Translational readthrough potential
622 of natural termination codons in eucaryotes – The impact of RNA sequence. *RNA Biol*
623 12: 950–958
624 El-Agnaf OMA, Nagala S, Patel BP & Austen BM (2001a) Non-fibrillar oligomeric species of
625 the amyloid ABri peptide, implicated in familial British dementia, are more potent at
626 inducing apoptotic cell death than protofibrils or mature fibrils11Edited by J. Karn. *J Mol*
627 *Biol* 310: 157–168
628 El-Agnaf OMA, Sheridan JM, Sidera C, Siligardi G, Hussain R, Haris PI & Austen BM
629 (2001b) Effect of the Disulfide Bridge and the C-Terminal Extension on the
630 Oligomerization of the Amyloid Peptide ABri Implicated in Familial British Dementia.
631 *Biochemistry* 40: 3449–3457
632 Faure AJ, Schmiedel JM, Baeza-Centurion P & Lehner B (2020) DiMSum: an error model
633 and pipeline for analyzing deep mutational scanning data and diagnosing common
634 experimental pathologies. *Genome Biol* 21: 207
635 Fernandez-Escamilla A-M, Rousseau F, Schymkowitz J & Serrano L (2004) Prediction of
636 sequence-dependent and mutational effects on the aggregation of peptides and
637 proteins. *Nat Biotechnol* 22: 1302–1306
638 Floquet C, Hatin I, Rousset J-P & Bidou L (2012) Statistical Analysis of Readthrough Levels
639 for Nonsense Mutations in Mammalian Cells Reveals a Major Determinant of Response
640 to Gentamicin. *PLoS Genet* 8: e1002608
641 Frazer J, Notin P, Dias M, Gomez A, Min JK, Brock K, Gal Y & Marks DS (2021) Disease
642 variant prediction with deep generative models of evolutionary data. *Nature* 599: 91–95
643 Ghiso JA, Holton J, Miravalle L, Calero M, Lashley T, Vidal R, Houlden H, Wood N, Neubert
644 TA, Rostagno A, *et al* (2001) Systemic Amyloid Deposits in Familial British Dementia.
645 *Journal of Biological Chemistry* 276: 43909–43914
646 Gibson G, Gunasekera N, Lee M, Lelyveld V, El-Agnaf OMA, Wright A & Austen B (2003)
647 Oligomerization and neurotoxicity of the amyloid ADan peptide implicated in familial
648 Danish dementia. *J Neurochem* 88: 281–290
649 Hamby SE, Thomas NS, Cooper DN & Chuzhanova N (2011) A meta-analysis of single
650 base-pair substitutions in translational termination codons ('nonstop' mutations) that
651 cause human inherited disease. *Hum Genomics* 5: 241
652 Holton JL, Ghiso J, Lashley T, Rostagno A, Guerin CJ, Gibb G, Houlden H, Ayling H,
653 Martinian L, Anderton BH, *et al* (2001) Regional Distribution of Amyloid-Bri Deposition
654 and Its Association with Neurofibrillary Degeneration in Familial British Dementia. *Am J*
655 *Pathol* 158: 515–526
656 Humphrey W, Dalke A & Schulten K (1996) VMD: Visual molecular dynamics. *J Mol Graph*
657 14: 33–38
658 Jumper J, Evans R, Pritzel A, Green T, Figurnov M, Ronneberger O, Tunyasuvunakool K,
659 Bates R, Žídek A, Potapenko A, *et al* (2021) Highly accurate protein structure prediction
660 with AlphaFold. *Nature* 596: 583–589

Kyte J & Doolittle RF (1982) A simple method for displaying the hydropathic character of a protein. *J Mol Biol* 157: 105–132

Lashley T, Holton JL, Verbeek MM, Rostagno A, Bojsen-Møller M, David G, van Horssen J, Braendgaard H, Plant G, Frangione B, *et al* (2006) Molecular chaperons, amyloid and preamyloid lesions in the BRI2 gene-related dementias: a morphological study. *Neuropathol Appl Neurobiol* 32: 492–504

Lin Z, Akin H, Rao R, Hie B, Zhu Z, Lu W, Smetanin N, Verkuil R, Kabeli O, Shmueli Y, *et al* (2023) Evolutionary-scale prediction of atomic-level protein structure with a language model. *Science (1979)* 379: 1123–1130

Liu X, Chen K-L, Wang Y, Huang Y-Y, Chen S-D, Dong Q, Cui M & Yu J-T (2021) A Novel ITM2B Mutation Associated with Familial Chinese Dementia. *Journal of Alzheimer's Disease* 81: 499–505

Madeira F, Pearce M, Tivey ARN, Basutkar P, Lee J, Edbali O, Madhusoodanan N, Kolesnikov A & Lopez R (2022) Search and sequence analysis tools services from EMBL-EBI in 2022. *Nucleic Acids Res* 50: W276–W279

Marcora MS, Fernández-Gamba AC, Avendaño LA, Rotondaro C, Podhajcer OL, Vidal R, Morelli L, Ceriani MF & Castaño EM (2014) Amyloid peptides ABri and ADan show differential neurotoxicity in transgenic Drosophila models of familial British and Danish dementia. *Mol Neurodegener* 9: 5

Mignogna ML, Ficarella R, Gelmini S, Marzulli L, Ponzi E, Gabellone A, Peschechera A, Alessio M, Margari L, Gentile M, *et al* (2022) Clinical characterization of a novel *RAB39B* nonstop mutation in a family with ASD and severe ID causing RAB39B downregulation and study of a *Rab39b* knock down mouse model. *Hum Mol Genet* 31: 1389–1406

Mirdita M, Schütze K, Moriwaki Y, Heo L, Ovchinnikov S & Steinegger M (2022) ColabFold: making protein folding accessible to all. *Nat Methods* 19: 679–682

Mompeán M, Li W, Li J, Laage S, Siemer AB, Bozkurt G, Wu H & McDermott AE (2018) The Structure of the Necrosome RIPK1-RIPK3 Core, a Human Hetero-Amyloid Signaling Complex. *Cell* 173: 1244-1253.e10

Monaghan L, Longman D & Cáceres JF (2023) Translation-coupled mRNA quality control mechanisms. *EMBO J*

Ng PC & Henikoff S (2001) Predicting Deleterious Amino Acid Substitutions. *Genome Res* 11: 863–874

Pickford F, Coomaraswamy J, Jucker M & McGowan E (2006) Modeling Familial British Dementia in Transgenic Mice. *Brain Pathology* 16: 80–85

Rebelo AP, Abrams AJ, Cottenie E, Horga A, Gonzalez M, Bis DM, Sanchez-Mejias A, Pinto M, Buglo E, Markel K, *et al* (2016) Cryptic Amyloidogenic Elements in the 3′ UTRs of Neurofilament Genes Trigger Axonal Neuropathy. *The American Journal of Human Genetics* 98: 597–614

Rhyu J-M, Park J, Shin B-S, Kim Y-E, Kim E-J, Kim KW & Cho YG (2023) A Novel c.800G>C Variant of the ITM2B Gene in Familial Korean Dementia. *Journal of Alzheimer's Disease* 93: 403–409

Scheller JS, Irvine GW & Stillman MJ (2018) Unravelling the mechanistic details of metal binding to mammalian metallothioneins from stoichiometric, kinetic, and binding affinity data. *Dalton Transactions* 47: 3613–3637

Schlenzig D, Manhart S, Cinar Y, Kleinschmidt M, Hause G, Willbold D, Funke SA, Schilling S & Demuth H-U (2009) Pyroglutamate Formation Influences Solubility and Amyloidogenicity of Amyloid Peptides. *Biochemistry* 48: 7072–7078

Seuma M & Bolognesi B (2022) Understanding and evolving prions by yeast multiplexed assays. *Curr Opin Genet Dev* 75: 101941

Seuma M, Faure AJ, Badia M, Lehner B & Bolognesi B (2021) The genetic landscape for amyloid beta fibril nucleation accurately discriminates familial Alzheimer's disease mutations. *Elife* 10

Seuma M, Lehner B & Bolognesi B (2022) An atlas of amyloid aggregation: the impact of substitutions, insertions, deletions and truncations on amyloid beta fibril nucleation. *Nat Commun* 13: 7084

Sormanni P, Aprile FA & Vendruscolo M (2015) The CamSol Method of Rational Design of Protein Mutants with Enhanced Solubility. *J Mol Biol* 427: 478–490

Tamayev R, Giliberto L, Li W, d'Abramo C, Arancio O, Vidal R & D'Adamio L (2010a) Memory Deficits Due to Familial British Dementia *BRI2* Mutation Are Caused by Loss of *BRI2* Function Rather than Amyloidosis. *The Journal of Neuroscience* 30: 14915–14924

Tamayev R, Matsuda S, Fà M, Arancio O & D'Adamio L (2010b) Danish dementia mice suggest that loss of function and not the amyloid cascade causes synaptic plasticity and memory deficits. *Proceedings of the National Academy of Sciences* 107: 20822–20827

Tesei G & Lindorff-Larsen K (2023) Improved predictions of phase behaviour of intrinsically disordered proteins by tuning the interaction range. *Open Research Europe* 2: 94

Tesei G, Trolle AI, Jonsson N, Betz J, Pesce F, Johansson KE & Lindorff-Larsen K (2023) Conformational ensembles of the human intrinsically disordered proteome: Bridging chain compaction with function and sequence conservation. *bioRxiv*: 2023.05.08.539815

Todd K, Fossati S, Ghiso J & Rostagno A (2014) Mitochondrial dysfunction induced by a post-translationally modified amyloid linked to a familial mutation in an alternative model of neurodegeneration. *Biochimica et Biophysica Acta (BBA) - Molecular Basis of Disease* 1842: 2457–2467

Todd K, Ghiso J & Rostagno A (2016) Oxidative stress and mitochondria-mediated cell death mechanisms triggered by the familial Danish dementia ADan amyloid. *Neurobiol Dis* 85: 130–143

Toledano I, Supek F & Lehner B (2023) Genome-scale quantification and prediction of pathogenic stop codon readthrough by small molecules. *bioRxiv*: 2023.08.07.552350

Vaché C, Cubedo N, Mansard L, Sarniguet J, Baux D, Faugère V, Baudoin C, Moclyn M, Touraine R, Lina-Granade G, *et al* (2023) Identification and in vivo functional investigation of a HOMER2 nonstop variant causing hearing loss. *European Journal of Human Genetics* 31: 834–840

Vidal R, Barbeito AG, Miravalle L & Ghetti B (2009) Cerebral Amyloid Angiopathy and Parenchymal Amyloid Deposition in Transgenic Mice Expressing the Danish Mutant Form of Human BRI $_2$. *Brain Pathology* 19: 58–68

Vidal R, Frangione B, Rostagno A, Mead S, Révész T, Plant G & Ghiso J (1999) A stop-codon mutation in the BRI gene associated with familial British dementia. *Nature* 399: 776–781

Vidal R, Révész T, Rostagno A, Kim E, Holton JL, Bek T, Bojsen-Møller M, Braendgaard H, Plant G, Ghiso J, *et al* (2000) A decamer duplication in the 3′ region of the *BRI* gene originates an amyloid peptide that is associated with dementia in a Danish kindred. *Proceedings of the National Academy of Sciences* 97: 4920–4925

Figures Legends

Figure 1. Amyloid nucleation of Bri2, ABri and Adan. A. Schematics of *Bri2 gene* and dementia-related mutations at the nucleotide and protein level. cDNA coordinates are detailed at the top and stop codons (conventional or alternative) are represented with bold fonts and upper case. The exon and its translated protein product is highlighted in purple. Extended products resulting from mutations are highlighted in yellow (ABri and ABri-like) and orange (Adan). Familial dementia mutations are detailed over the arrows. **B.** Relative growth of cells expressing Bri2, ABri or ADan fusions calculated as number of colonies growing in the selective conditions of the amyloid nucleation assay (-URA–Ade) over colonies growing in the absence of selection (-URA) (Chandramowlishwaran *et al*, 2018). Error bars indicate the standard deviation of the experiments (n=3).
C. Deep mutagenesis scheme. A library of sequences of interest is expressed in yeast and selected for amyloid nucleation as reported in (Seuma *et al*, 2021). Amyloid nucleation scores are obtained through deep sequencing of input and output samples.
D. ADan truncations nucleation propensity. The horizontal line indicates the weighted mean nucleation score of Bri2 truncations (up to position 22). Vertical error bars indicate 95% confidence interval of the mean.

Figure 1. Deep mutagenesis of ADan. A. Correlation of nucleation scores between two biological replicates for variants in the ADan library. Pearson correlation and p-value are indicated. **B.** Correlation between nucleation scores obtained from selection and deep sequencing and relative growth of individual variants in selective conditions (n=5). Vertical and horizontal error bars indicate sigma errors. Pearson correlation and p-values are indicated. **C.** Distribution of nucleation scores for each class of mutations in ADan library. **D.** Frequency of variants increasing or decreasing nucleation at FDR=0.1 and variants that are WT-like. **E.** Heatmap of nucleation scores for ADan single AA substitutions. The WT AA and position are indicated in the x-axis and the mutant AA is indicated in the y-axis. Synonymous variants are indicated as “ADan”, missense variants due to SNVs are indicated with “\” and SNVs present in GnomAD with a “\\” in the upper right corner of the cell. The distribution of nucleation scores for each position is summarized in the violin plots below the heatmap. The number of variants increasing or decreasing nucleation at FDR=0.1 per position are indicated as stack bars at the bottom. The distribution of nucleation scores for each mutation is summarized in the violin plots at the right-hand side of the heatmap. The number of variants increasing or decreasing nucleation at FDR=0.1 per mutation are indicated as stack bars at the right. **F.** Frequency of single AA substitutions that are increasing or decreasing nucleation (FDR=0.1) upon substituting specific WT AA.

Figure 3. Deep mutagenesis of ABri. A. Correlation of nucleation scores between two biological replicates for variants in the ABri library. Pearson correlation and p-value are indicated. B. Correlation of nucleation scores obtained from selection and deep sequencing with relative growth of individual variants in selective conditions (n=3).

800 Vertical and horizontal error bars indicate sigma errors. Pearson correlation and p-
801 values are indicated. C. Heatmap of nucleation scores for ABri single AA
802 substitutions. The WT AA and position are indicated in the x-axis and the mutant AA
803 is indicated in the y-axis. Synonymous variants are indicated as "ABri", missense
804 variants due to SNVs are indicated with "\" and SNVs present in GnomAD with a "\\" in
805 the upper right corner of the cell. Missing variants have been excluded on the basis of
806 poor sequencing quality and low normalized sigma values (see Methods).
807
808 **Figure 4. Comparing the mutational effects of single AA variants in ADan, Aβ42**
809 **and ABri libraries. A-B.** Correlation of average nucleation scores for each type of
810 substitution of the same AA (A) or to the same AA (B) in Adan and Aβ42. **C.** Correlation
811 of average nucleation scores per AA change between ADan and Aβ42. Points are
812 colored on the basis of the type of change. **D-E.** Correlation of average nucleation
813 scores for each substitution to the same AA (D) or of the same AA (E) in Adan and
814 ABri. **F.** Correlation of ADan and ABri nucleation scores for positions with more than 4
815 values in ABri library. ADan residues are detailed in orange and ABri residues in red.
816 Pearson correlation and p-value are indicated in each plot.
817
818 **Supplementary Figure 1. ADan and ABri nucleation. A.** Inidvidual testing of SupN
819 (negative control), Aβ42 (positive control), Bri2, ABri and ADan in the reporter assay.
820 T-test significance is indicated. **C.** Correlation of nucleation scores between biological
821 replicates for variats in the ADan library. Pearson correlation and p-value are
822 indicated. **B.** Normalized Sigma distribution for variants increasing, decreasing or not
823 affecting nucleation at FDR=0.1. Vertical line indicates threshold value for considering
824 low sigma. **D.** Correlation of nucleation scores between biological replicates for
825 variants in the ABri library. Pearson correlation and p-value are indicated.
826
827 **Supplementary Figure 2. Mutational effects of single AA substitutions.** Heatmap
828 of FDR categories for the effects of single AA substitutions. The WT AA and position
829 are indicated in the x-axis and the mutant AA is indicated in the y-axis. Synonymous
830 mutants are indicated with "ADan" (**A**) or "ABri" (**B**). Missense variants due to SNVs
831 present in GnomAD are indicated with "\" in the upper right corner of the cell. The
832 number of variants increasing or decreasing nucleation at different FDRs per position
833 are indicated as stack bars at the bottom.
834
835 **Supplementary Figure 3. Comparing the mutational effects of single amino acid**
836 **variants in ADan, Aβ42 and ABri libraries.** Correlation of nucleation scores between
837 ADan and Aβ42 aligned at N-term (**A**), at C-term (**B**) and with ClustalO (**C**), and
838 between ADan and ABri (**D**).
839
840 **Supplementary Figure 4. Structural insights into Bri2, ABri and ADan. A.** Bri2,
841 ABri and ADan structure prediction by Alphafold and MetaESM. Model confidence is
842 colored with a divergent palette: Blue = High, Green = Mid and Red = Low. **B.** Non-

843 ionic energy contact maps of Bri2, ABri and ADan calculated with CALVADOS force-
844 field. Color scale indicates the interaction energy between residues.
845
846 **Supplementary Figure 5. Physicochemical features partially explain nucleation.**
847 **A.** ADan nucleation scores correlation with amyloid propensity predictors (Tango and
848 Amypred), solubility predictors (CamSol) and Kyte-Doolittle hydrophobicty score. Red
849 dots indicate the values for the WT sequence. Pearson correlation and p-values are
850 indicated. **B.** Nucleation score distributions arranged by the number of charged
851 residues (y-axis) and the total net charge (x-axis) in ADan. Numbers inside each cell
852 indicate the number of positive and negative residues. The horizontal line indicates
853 WT nucleation score (0).

Supplementary Table 1. SNVs in Bri2 gene reported in GnomAD database.

ID	HGSVc	HGVS Bri2	HGVS ABri	HGVS ADan	AF	NS ABri	NS ADan
rs1425712363	c.730G>A	p.Glu244Lys	p.Glu1Lys	p.Glu1Lys	3.99e-6	-	-1.20
rs1302882644	c.737G>A	p.Ser246Asn	p.Ser3Asn	p.Ser3Asn	3.99e-6	-	0.0448
rs1365902742	c.743G>A	p.Cys248Tyr	p.Cys5Tyr	p.Cys5Tyr	3.99e-6	-	-0.00901
rs765077508	c.747C>G	p.Phe249Leu	p.Phe6Leu	p.Phe6Leu	3.99e-6	-0.109	-0.500
rs578006622	c.748G>T	p.Ala250Ser	p.Ala7Ser	p.Ala7Ser	4.38e-5	0.962	0.0708
rs578006622	c.748G>A	p.Ala250Thr	p.Ala7Thr	p.Ala7Thr	7.97e-6	-	-0.0425
rs139394220	c.751A>G	p.Ile251Val	p.Ile8Val	p.Ile8Val	1.24e-4	1.31	0.0841
rs1272422512	c.755G>A	p.Arg252Gln	p.Arg9Gln	p.Arg9Gln	1.20e-5	-	0.474
rs1380885043	c.769A>G	p.Lys257Glu	p.Lys14Glu	p.Lys14Glu	6.37e-5	-	-0.00624
rs1290822136	c.776C>T	p.Ala259Val	p.Ala16Val	p.Ala16Val	7.97e-6	-	-0.233
rs373968526	c.778G>A	p.Val260Met	p.Val17Met	p.Val17Met	1.59e-5	-	-1.07
rs1428007068	c.787T>G	p.Leu263Val	p.Leu20Val	p.Leu20Val	3.99e-6	-	-1.46
rs747798420	c.788T>C	p.Leu263Ser	p.Leu20Ser	p.Leu20Ser	7.97e-6	1.84	-3.53
rs771676204	c.790A>G	p.Ile264Val	p.Ile21Val	p.Ile21Val	3.99e-6	0.211	-0.0338
rs772731795	c.*3A>G	-	p.Thr25Thr	p.Ser29Gly	3.99e-6	-	-0.160
rs1163491396	c.*8A>G	-	p.Lys27Arg	p.Gln30Gln	3.99e-6	0.343	-
rs760120359	c.*11A>G	-	p.Lys28Arg	p.Glu31Glu	1.20e-5	0.873	-
rs1455609180	c.*13A>C	-	p.Asn29His	p.Lys32Thr	4.00e-6	-	0.234
rs770862229	c.*15C>T	-	p.Asn29Asn	p.His33Tyr	4.00e-6	-	-0.228
rs776617945	c.*18T>C	-	p.Ile30Ile	p. Tyr34His	4.00e-6	-	0.0246
rs759493813	c.*20T>C	-	p.Ile31Thr	p. Tyr34Tyr	7.10e-6	-	-

Figure 1

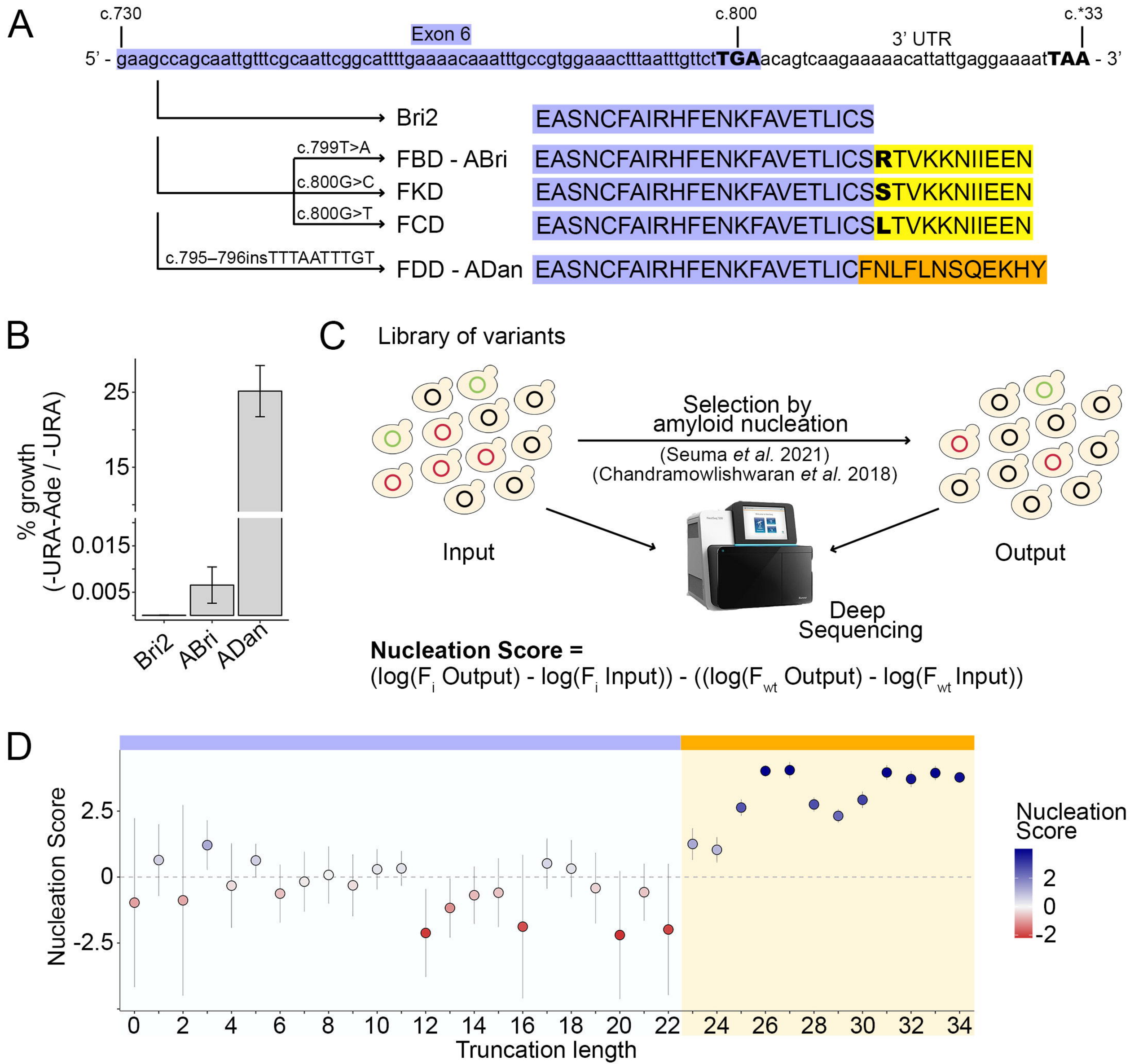
A
c.730
Exon 6
c.800
3' UTR
c.*33
5' - gaagccagcaattgtttcgcaattcggcattttgaaaacaaatttgccgtggaaactttaatttgttctTGAacagtcaagaaaaacattattgaggaaaatTAA - 3'
Bri2
EASNCFAIRHFENKFAVETLICS
c.799T>A
FBD - ABri
EASNCFAIRHFENKFAVETLICSRTVKKNIIEEN
c.800G>C
FKD
EASNCFAIRHFENKFAVETLICSSTVKKNIIEEN
c.800G>T
FCD
EASNCFAIRHFENKFAVETLICSLTVKKNIIEEN
c.795–796insTTTAATTTGT
FDD - ADan
EASNCFAIRHFENKFAVETLICFNLFLNSQEKHY
B
% growth
(-URA-Ade / -URA)
25
15
0.015
0.005
Bri2
ABri
ADan
C
Library of variants
Selection by
amyloid nucleation
(Seuma et al. 2021)
(Chandramowlishwaran et al. 2018)
Input
Output
Deep
Sequencing
Nucleation Score =
(log(F_i Output) - log(F_i Input)) - ((log(F_wt Output) - log(F_wt Input))
D
Nucleation Score
2.5
0
-2.5
0
2
4
6
8
10
12
14
16
18
20
22
24
26
28
30
32
34
Truncation length
Nucleation
Score
2
0
-2

Figure 2

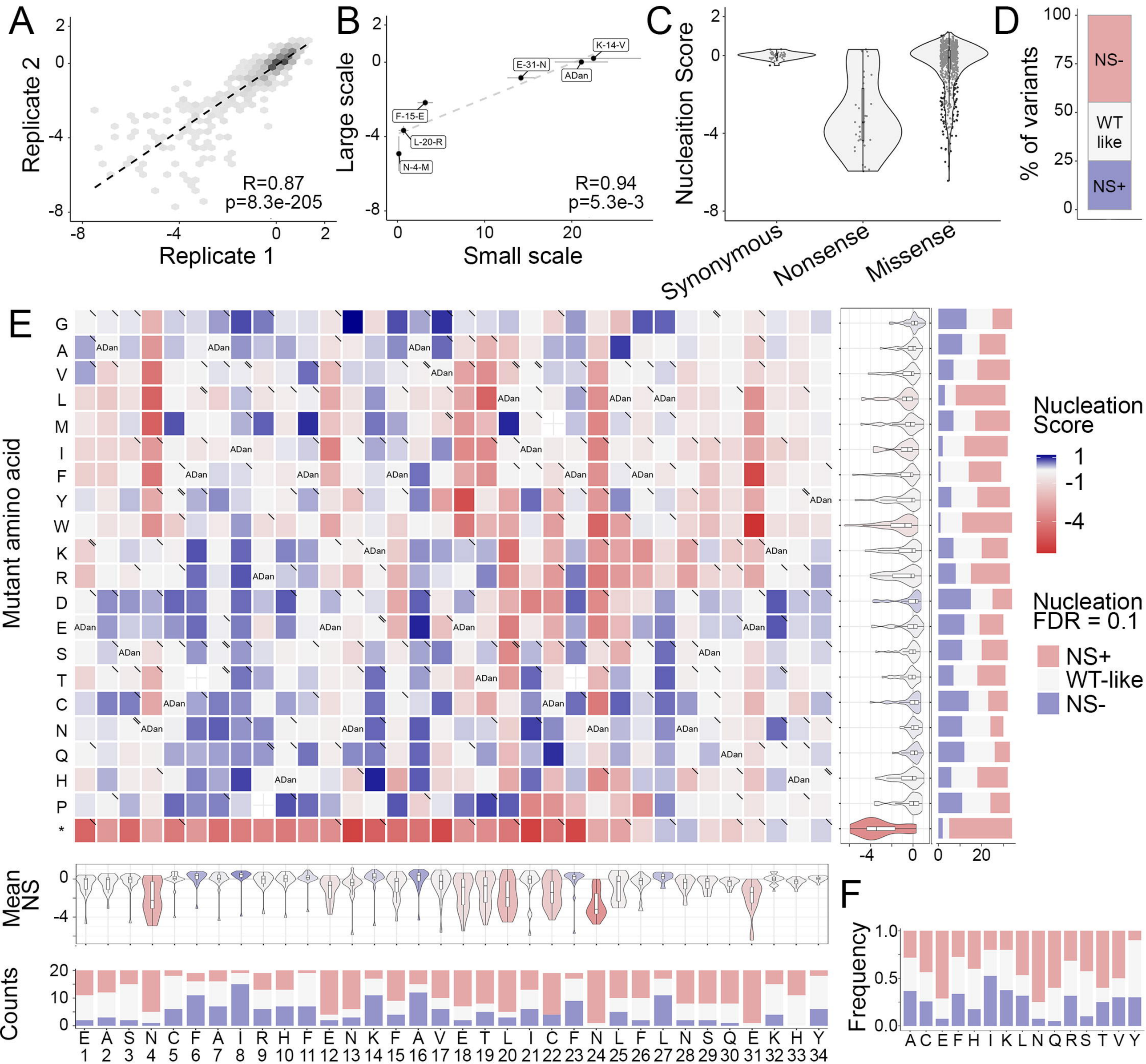
A
Replicate 2
Replicate 1
R=0.87
p=8.3e-205
B
Large scale
Small scale
R=0.94
p=5.3e-3
K-14-V
E-31-N
ADan
F-15-E
L-20-R
N-4-M
C
Nucleaition Score
Synonymous
Nonsense
Missense
D
% of variants
NS-
WT like
NS+
E
Mutant amino acid
Nucleation Score
Nucleation FDR = 0.1
NS+
WT-like
NS-
Mean NS
Counts
F
Frequency

Figure 3

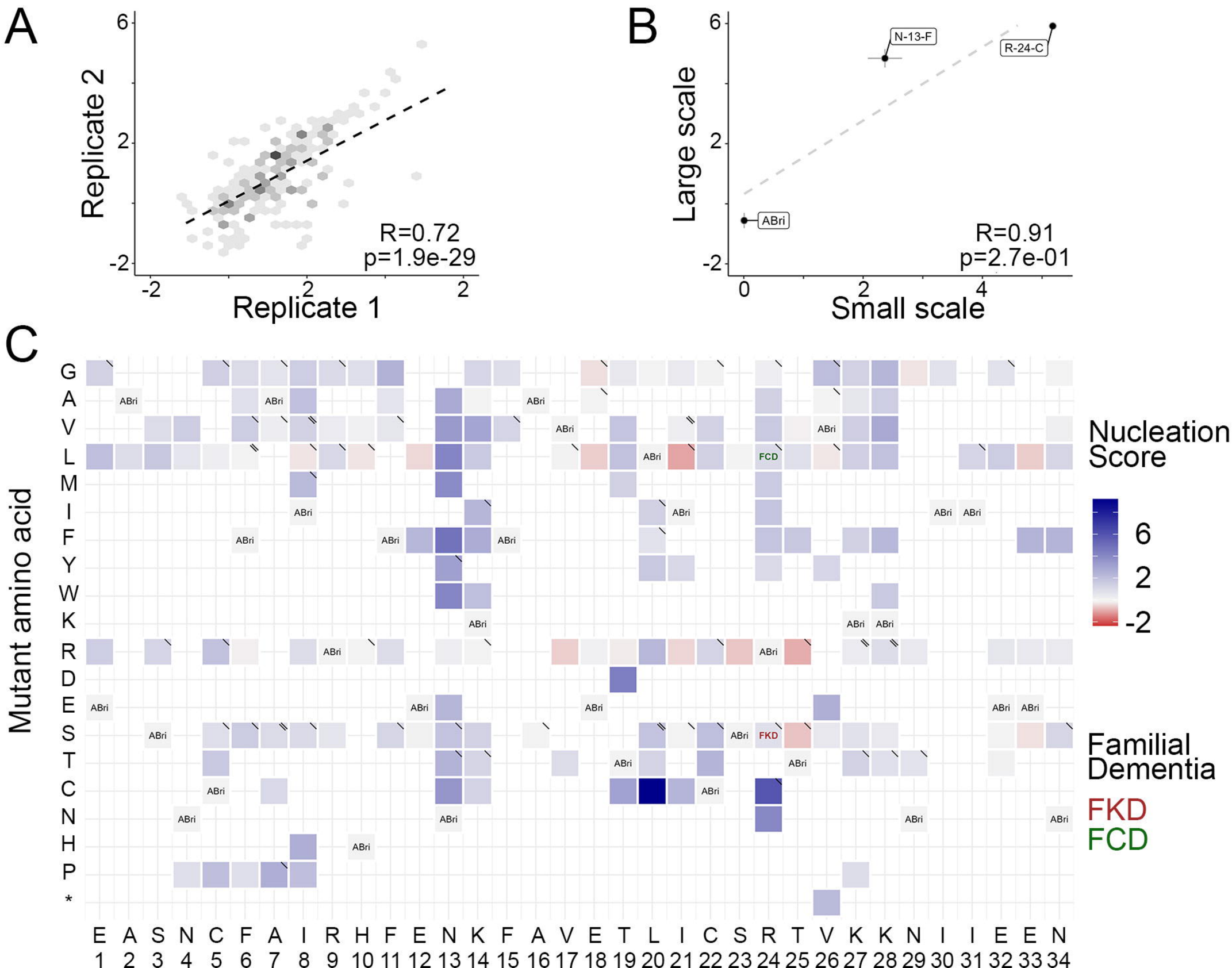
A
Replicate 2
Replicate 1
R=0.72
p=1.9e-29
B
Large scale
Small scale
N-13-F
R-24-C
ABri
R=0.91
p=2.7e-01
C
Mutant amino acid
G
A
V
L
M
I
F
Y
W
K
R
D
E
S
T
C
N
H
P
*
E 1 A 2 S 3 N 4 C 5 F 6 A 7 I 8 R 9 H 10 F 11 E 12 N 13 K 14 F 15 A 16 V 17 E 18 T 19 L 20 I 21 C 22 S 23 R 24 T 25 V 26 K 27 K 28 N 29 I 30 I 31 E 32 E 33 N 34
ABri
FCD
FKD
Nucleation Score
Familial Dementia
FKD
FCD

Figure 4

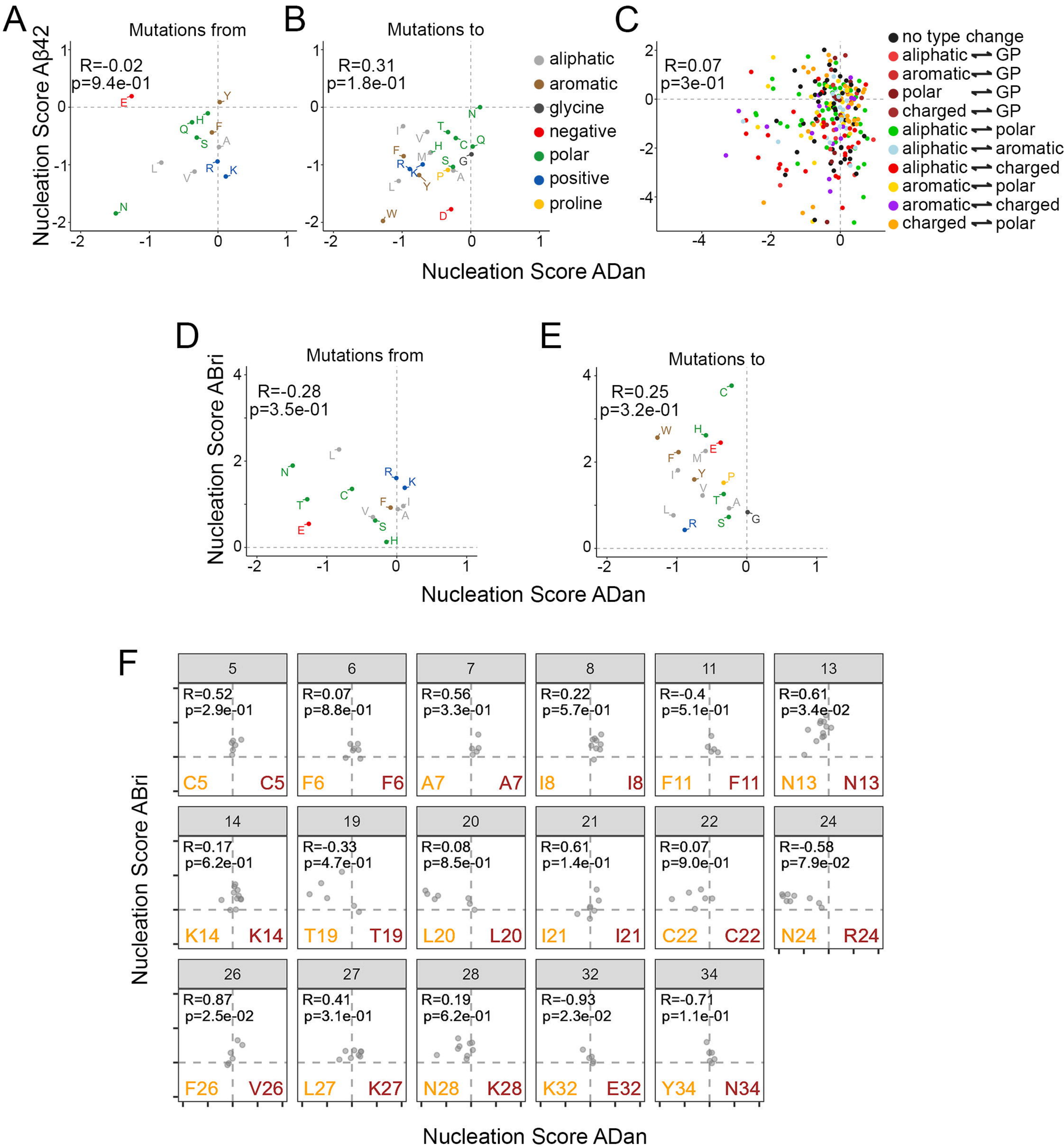
A
Mutations from
R=-0.02
p=9.4e-01
Nucleation Score Aβ42
B
Mutations to
R=0.31
p=1.8e-01
aliphatic
aromatic
glycine
negative
polar
positive
proline
C
R=0.07
p=3e-01
no type change
aliphatic ⇄ GP
aromatic ⇄ GP
polar ⇄ GP
charged ⇄ GP
aliphatic ⇄ polar
aliphatic ⇄ aromatic
aliphatic ⇄ charged
aromatic ⇄ polar
aromatic ⇄ charged
charged ⇄ polar
Nucleation Score ADan
D
Mutations from
R=-0.28
p=3.5e-01
Nucleation Score ABri
E
Mutations to
R=0.25
p=3.2e-01
Nucleation Score ADan
F
5
R=0.52
p=2.9e-01
C5 C5
6
R=0.07
p=8.8e-01
F6 F6
7
R=0.56
p=3.3e-01
A7 A7
8
R=0.22
p=5.7e-01
I8 I8
11
R=-0.4
p=5.1e-01
F11 F11
13
R=0.61
p=3.4e-02
N13 N13
14
R=0.17
p=6.2e-01
K14 K14
19
R=-0.33
p=4.7e-01
T19 T19
20
R=0.08
p=8.5e-01
L20 L20
21
R=0.61
p=1.4e-01
I21 I21
22
R=0.07
p=9.0e-01
C22 C22
24
R=-0.58
p=7.9e-02
N24 R24
26
R=0.87
p=2.5e-02
F26 V26
27
R=0.41
p=3.1e-01
L27 K27
28
R=0.19
p=6.2e-01
N28 K28
32
R=-0.93
p=2.3e-02
K32 E32
34
R=-0.71
p=1.1e-01
Y34 N34
Nucleation Score ABri
Nucleation Score ADan

Supplementary Figure 1

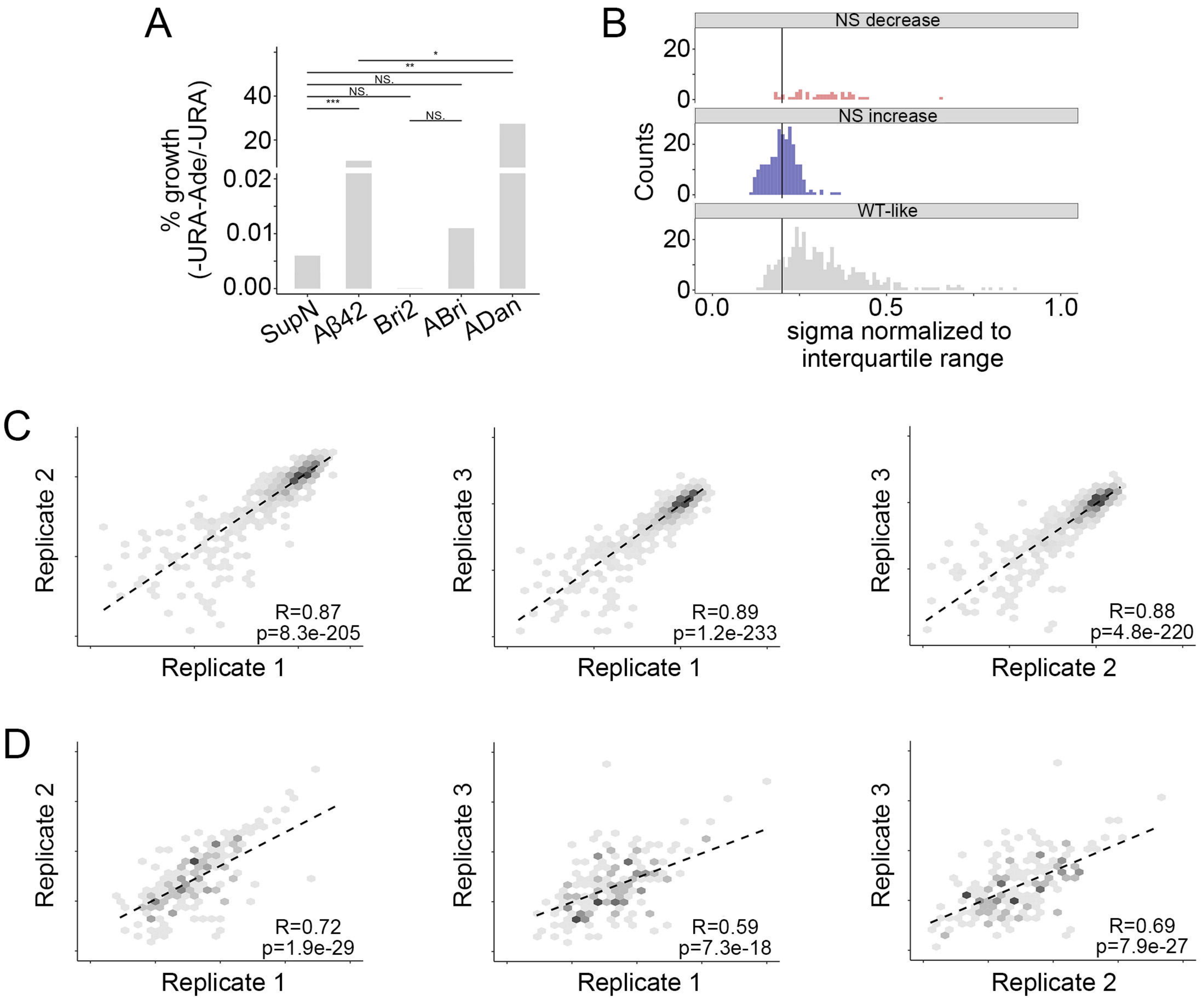

Supplementary Figure 2

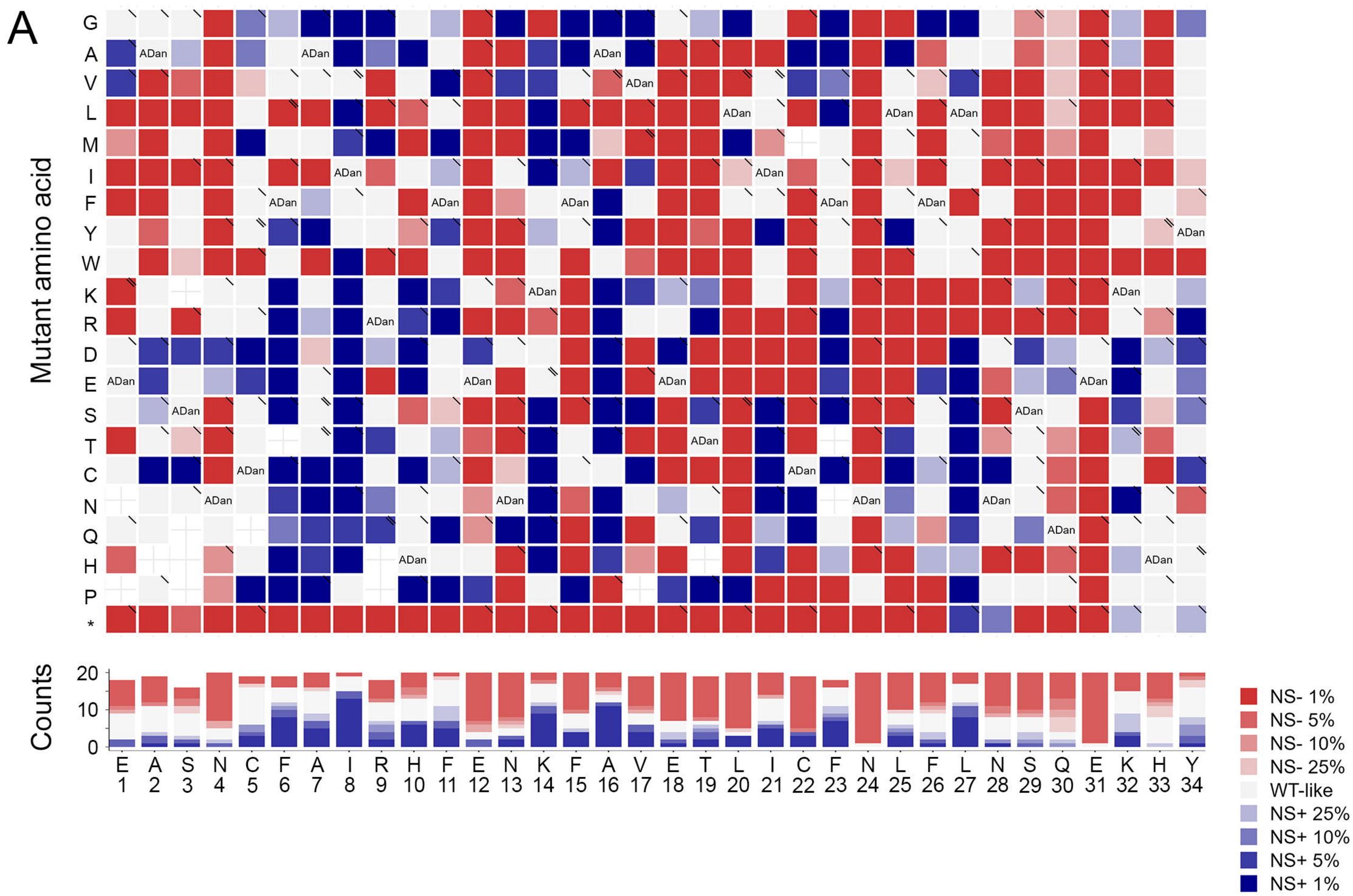

Supplementary Figure 3

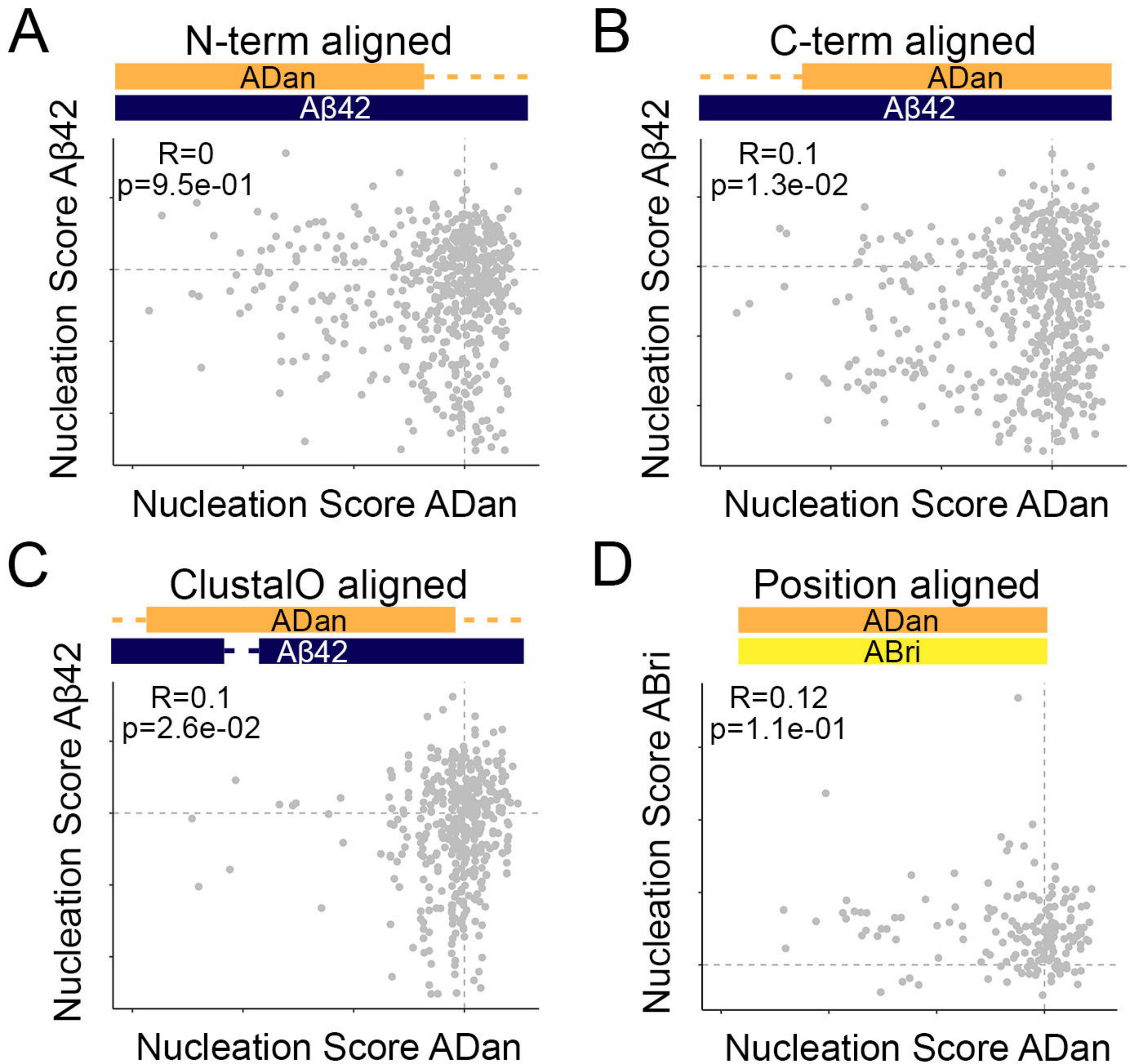

Supplementary Figure 4

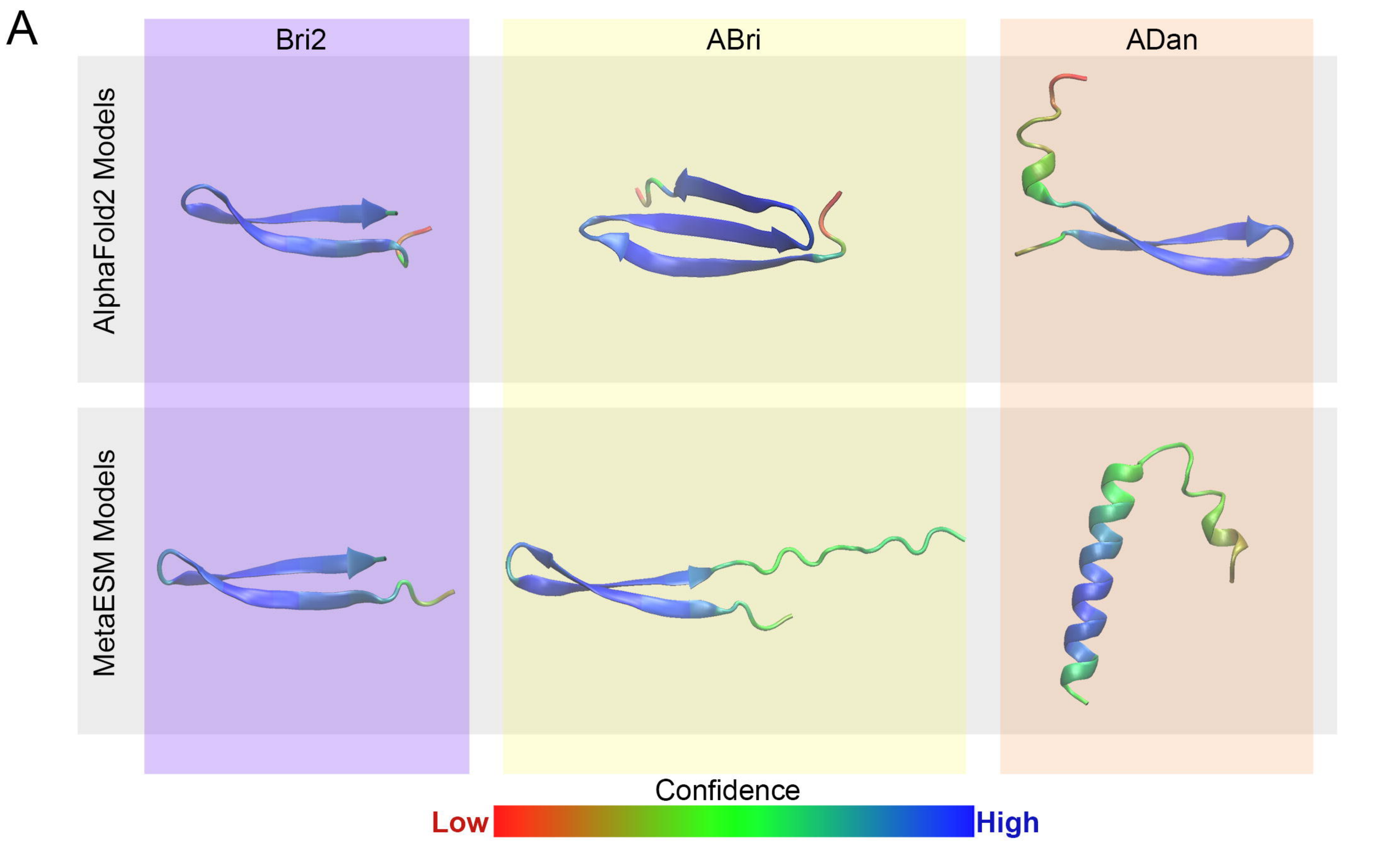

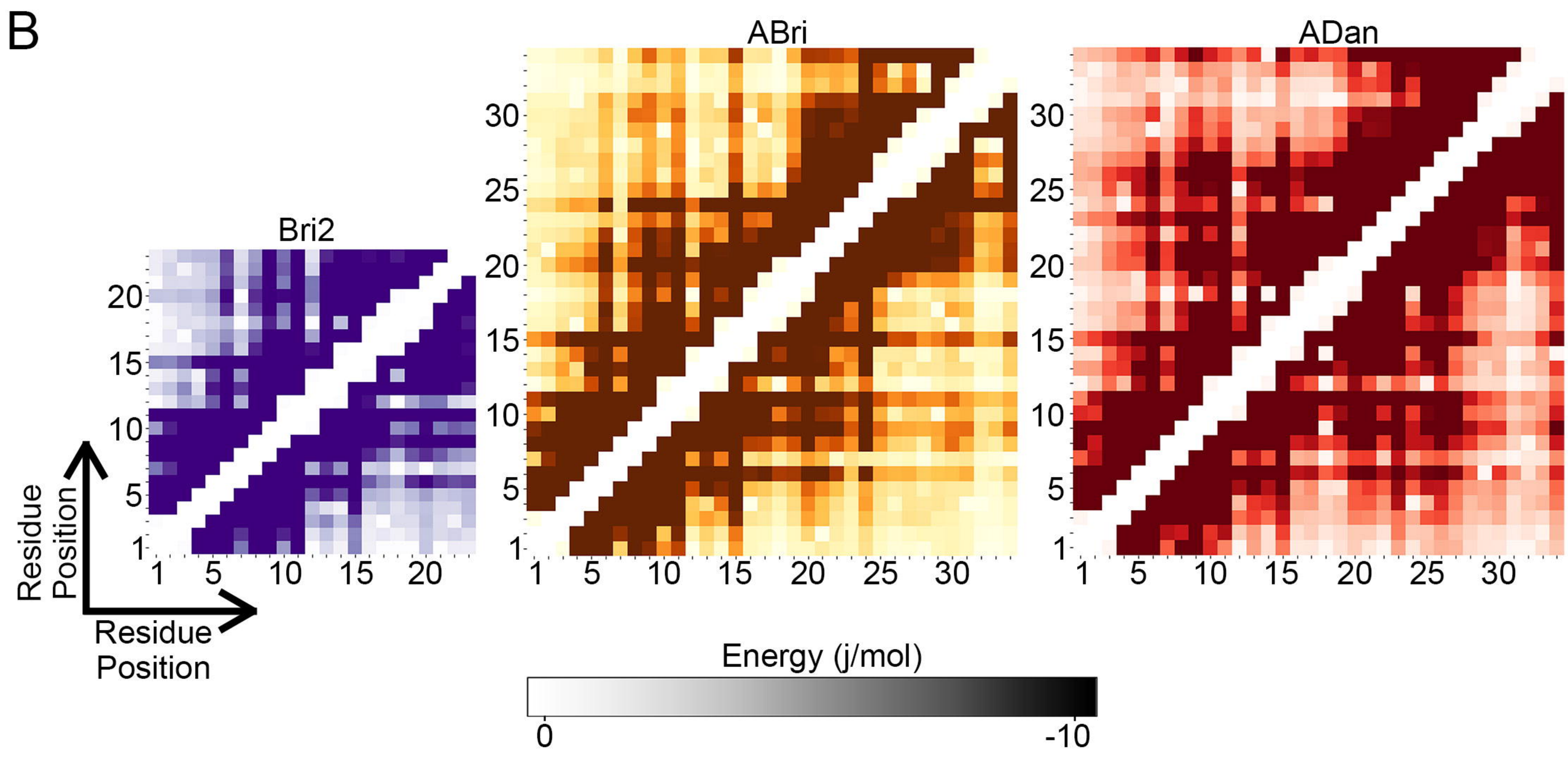
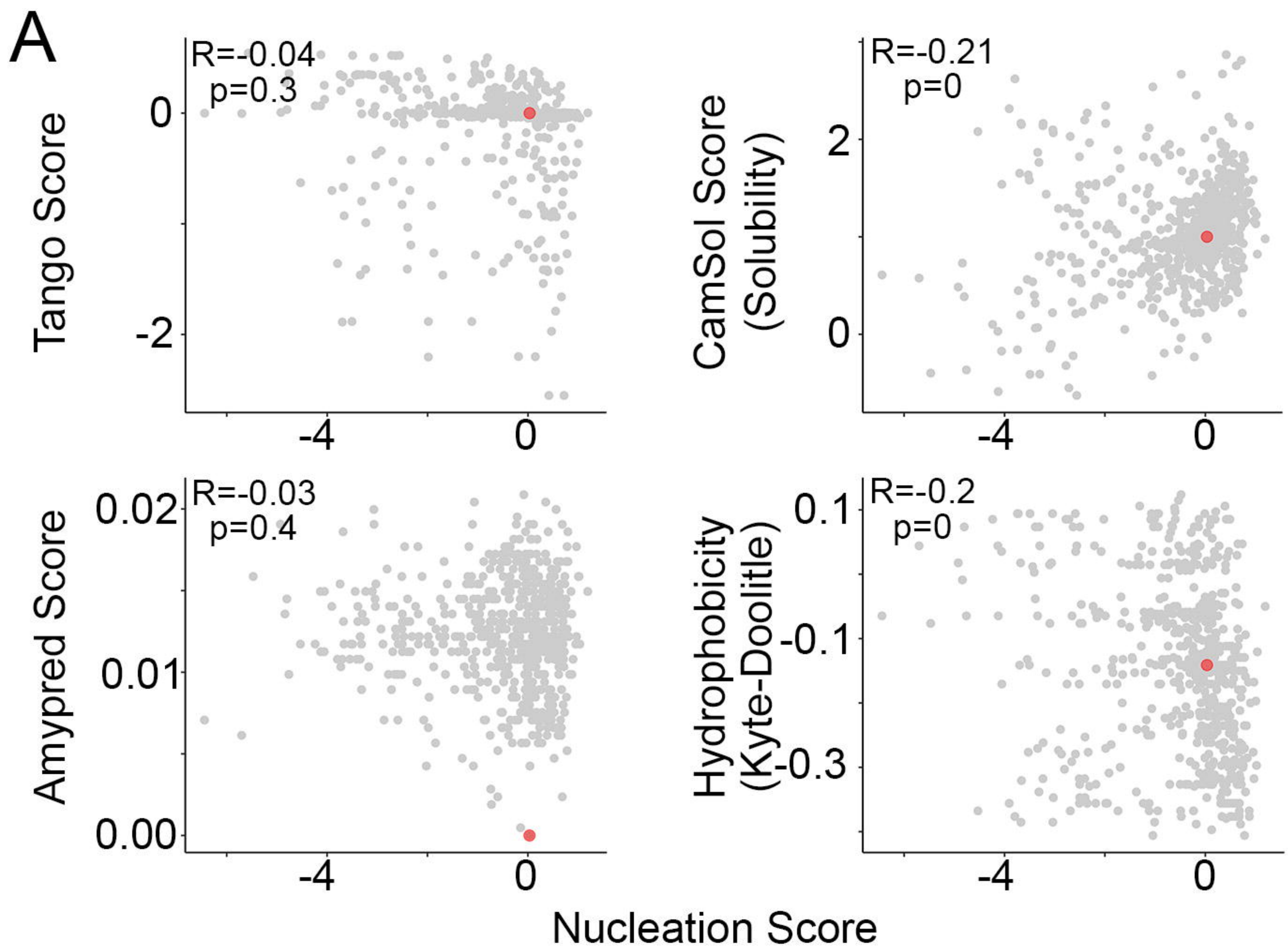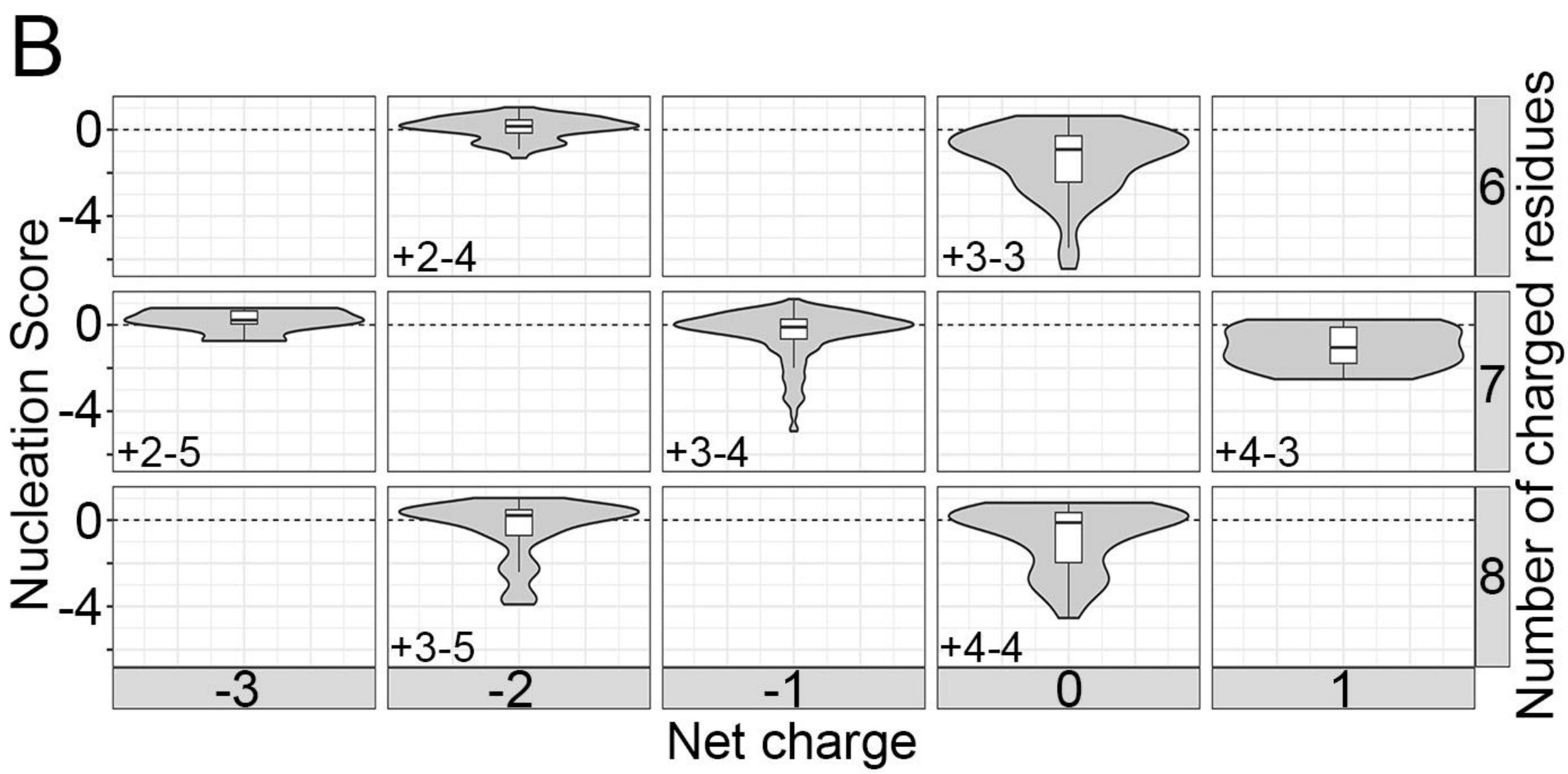
Supplementary Figure 5